Master's Thesis 2024

Nanowires and molecule-based memory systems for optically transmitted signal manipulation

Nathanael Löfström
na4762lo-s@student.lu.se
June 27, 2024

LUNDS
UNIVERSITET

Master's thesis work carried out at the Division of Synchrotron Radiation Research, Department of Physics, Lund University in the EU founded project InsectNeuroNano

Supervisor: **Anders Mikkelsen**, anders.mikkelsen@sljus.lu.se
Examiner: **Carina Fasth**, carina.fasth@ftf.lth.se

Contents

Abstract

With the rapid growth of AI and large language models, concerns about their energy consumption have become increasingly prominent. The traditional digital von Neumann architecture is ill-suited for deep neural networks, prompting the exploration of neuromorphic computational models. These models draw inspiration from nature and the brain to integrate memory and computation efficiently. This thesis, part of the EU-funded InsectNeuroNano project, aims to advance neuromorphic computing.

DASA molecules, a type of photoswitching dye, are used in this project to replicate synaptic weights between neurons. This enables light to act as a signal carrier, allowing the dye to calculate inter-neuron weights. The project investigates dye deposition on 1 cm $\times$ 1 cm sapphire slabs, measuring changes in transmission over time and fitting a kinetic decay model.

Additionally, this thesis explores the replication of biological neurons' abilities to receive excitatory and inhibitory signals, process them via a sigmoid activation function, and transmit outputs. As part of the InsectNeuroNano project, III-V nanowires have been combined to create a simple artificial neuron replicating these characteristics. Various measurements on these devices aim to demonstrate their ability to mimic the necessary properties of biological neurons. These measurements include electrical and photoelectrical aspects, divided into standardized and general tests.

The nanowire neuron circuits demonstrated vital properties such as inhibition, excitation, sigmoid activation, and pulse trains. However, these effects were not fully optimized, indicating a gap between biological and artificial neurons. Additional unexplained effects were also observed.

Only two samples fit the kinetic model for the dye experiments, with the other samples affected by irreversible bleaching and where the measurement continued to bleach them. The limited data prevented definitive conclusions about the deposition parameter space, though a potential pattern related to annealing was noted, warranting further investigation.

Acknowledgements

First, I would like to thank my supervisor, Anders Mikkelson, for allowing me to participate in this fascinating project. When I first heard of InsectNeroNano, I was fascinated, and the quick and warm welcome helped me get going. From the support and, later on, the inclusion in the conference, I warmly thank you.

From the first, I have also received help from Thomas K. Jensen, who, knowing how everything worked, showed me around and helped me understand how to measure on the devices. Without your help, this would probably have taken quite a lot longer.

I would also like to thank Abhijit, Vidar, Nelia, Mariia and David at Lund University and Joachim and Abbey at Copenhagen University for all their help, suggestions, discussions and pleasant conversations.

Finally, I would also like to thank all the others at the InsectNeuroNano who have helped me through discussions and those at Lund University who helped

me with equipment and explanations.

As always, a warm thank you to my family for everything which has enabled me, by God's grace, to complete this daunting and exciting journey.

Populärvetenskaplig sammanfattning

Det är sommar och fåglarna flyger kvickt genom luften, lekande i de varma vindbyarna. För insekterna är detta som vanligt, en kamp mot en fientlig värld och oräkneliga varelser som vill äta dem. Myrorna skyndar sig fram över varma stenar och mellan vegetation i jakt på något som kan tas tillbaka som mat. Varje myra är förbrukningsbar, enbart kolonin spelar roll. Men trots den snålheten med energi som detta leder till klarar de inte bara att hitta mat utan också att leta sig tillbaka till kolonin. Deras små hjärnor, arbetande med den energin som de har, lyckas navigera genom denna ogästvänliga och stora värld.

Gömd från sommarens hetta i den svalkande skuggan av en ek iakttar du myrorna. Men så väck en tanke. Är detta verkligen så imponerande? Har inte människan AI som med alla dess funktionaliteter och förmågor är vida överlägsna i intelligens hela myrornas kolonier? Svaret är inte riktigt så enkelt. AI klarar av att lösa många problem som är omöjliga för myrorna men har samtidigt stora begränsningar. AI, i all sin strålande ungdom, kräver mycket mer energi än insekter, något som blivit ett allt mer uppmärksammat problem. I förhållande har insekterna haft flera hundra miljoner år av evolution på sig att optimera sin intelligens.

I vad många kallar "age of AI" så har detta problem blivit allt mer framträdande och EU har genom olika projekt försökt finna lösningar. Denna uppsats är genomförd som en del av ett av dessa projekt, InsectNeuroNano, där målet är att skapa en fysisk kopia av insekternas navigationssystem. För att detta skall fungera krävs en bra förståelse över hur de planerade komponenterna fungerar vilket är där denna uppsats kommer in med sitt bidrag.

Genom forskning på insekter vid Lunds universitet har forskare kartlagt en region i deras hjärna kallad det centrala komplexet, som är ansvarigt för navigation. För att kunna efterlikna denna funktion har forskarna använt nanotrådar. Dessa är små pelare som mäter ungefär en hundradel av ett hårstrå i längd och en tusendel i tjocklek. Genom att kombinera nanotrådarna kan man efterlikna en neurons funktion, med målet att arrangera dem i en ring för att simulera insekternas signalsystem. De artificiella neuronerna använder ljus som signalbärare. Genom att justera deras placering kan forskarna styra hur ljuset interagerar med de olika neuronerna, vilket efterliknar hur signaler fördelas i en insekts hjärna. Den första delen av experimenten i denna uppsats syftar till att förstå hur ljus, nanotrådar och elektricitet samverkar, samt hur dessa artificiella neuroner kan härma biologiska neuroners egenskaper. En serie experiment har genomförts för att ta fram tre standardmätningar som avgör om en artificiell neuron har de egenskaper som krävs. I alla hjärnor, inklusive insekternas, finns något som kallas vikt mellan neuroner. Detta representerar hur många och hur starka signalerna mellan neuroner är, vilket gör det möjligt för insekterna att minnas. För att

implementera detta har forskarna använt ett färgämne som blir mer transparent när det exponeras för ljus. Om färgämnet sedan lämnas i mörker återfår det sin ursprungliga färg. Detta innebär att om färgämnet belyses ofta, på grund av många starka signaler mellan neuroner, kommer det att släppa igenom mer ljus. Olika experiment har genomförts där detta ämne blandats i plast och placerats på olika ytor. Förändringen av färg över tid har sedan mätts för att förstå hur placeringen påverkar återgångstiden. När resultaten sammanfattades visade det sig att både nanotrådarna och färgämnet kan hjälpa forskare att återskapa insekters hjärnfunktioner i datorer. Mycket mer forskning och förståelse krävs fortfarande, men framtiden med robotar som är lika intelligenta och små som insekter kanske inte är långt borta. Denna forskning visar ett hoppfullt budskap: vi behöver inte återuppfinna intelligens. Energieffektiviteten vi söker, simpliciteten och miljövänliga robotar är något som surrar runtomkring oss. Allt vi behöver är att luta oss tillbaka, njuta av sommarvärmen och beundra de små hjältarna som utan att veta om det kan vara de som, i all sin enkelhet, kommer lösa många av de problem som bekymrar våra bästa.

Abbreviations

- Nanowires = **NW**
- Biological neuron = **BN**
- Artificial neuron = **AN**
- Optical Beam-Induced Current = **OBIC**
- Artificial intelligence = **AI**
- Central complex = **CX**
- Donar-Acceptor Stenhouse Adduct dyes = **DASA**
- Ground state = **GS**
- Near infra-read = **NIR**
- Metastable = **M**
- Filed effect transistor = **FET**
- Indium Arsenic = **InAs**
- Indium Phosphide = **InP**

1 Introduction

Insects are everywhere in nature, often working in colonies where the individual is of little importance. In these environments, where predators come from all sides, and no one cares if an insect dies, a necessity to avoid wasting energy has been developed. A small ant should be able to go out and find food with minimal energy usage and still navigate back to its colony despite the large and unfriendly world in which it travels.

It is easy to assume that humans, with our advanced technologies and AI, could quickly reproduce the navigation ability of insects or even outperform them. This does, however, turn out not to be the case. Many of the abilities that insects or animals exhibit are either very costly and cumbersome or not feasible with today's technologies. So what problem have the insects solved that still evades us humans?

Insects have had roughly 450 million years of evolution to optimise their systems and specialise in what they need to do. It turns out that a part of the insect brain called the Central Complex [CX] exists with significant similarities between different species and is responsible for how they navigate[1]. It can be understood as a ring of neurons which, though localising the sensory input to a few neurons, can encode the direction towards home.

1.1 AI today

It is impossible to deny that society seems to have entered an AI revolution or, as some call it, the fourth industrial revolution, as it is part of the robotization of labour. AI has for some time been an everyday occurrence in the life of modern man; however, with the revealing of Chat-GTP, it exploded. In almost no time, Chat-GTP, along with other AI engines, has become a staple "expert" in studies and life in general. Not wanting to be left behind, a global race has started between companies to develop their interactive AI in programming, automatic cars and factory optimisation.

These models, though impressive in their scale and quick development, have a problem that has become increasingly prominent and is predicted to become the main limitation of AI in the future: the energy demand. In the worst case, a fully integrated AI-guided search engine for Google could consume the energy of Island yearly[2]. Already, Google reports that approximately 15 % of their total energy usage goes toward AI and machine learning. At the same time, it is noted that the computational power used in the largest AI training was doubled every 4 months between 2012 and 2022, increasing 6 times as quickly as Moor law [3]. Compared to an insect's brain, our models have several drawbacks. One is the specialisation of the insect's neurons, another is the energy efficiency of their brain compared to an artificial neural network, and another is the data reduction automatically happening in the insect sensors. The advantages of insects are not so surprising since they have had hundreds of millions of years to evolve, specialise, and find optimal energy use.

In comparison, training an AI on a supercomputer requires about the same energy as the human brain needs for everything it does over a 6-year period [4].

The prominent way to build an artificial neural network today is to use conventional computing through the von Neumann architecture. This architecture refers to when the computing unit and the memory are handled by two separate parts, and any data that needs to be stored or retrieved has to travel in between. This model has a specific limitation: the von Neumann bottleneck. The Neumann bottleneck refers to the increasing problem of data transfer between memory and CPU. When the data processing is fast enough, the limiting factor is how quickly data can be exchanged between CPU and memory. This is, unfortunately, limited by physics and cannot be solved by creating a more expensive computer [5].

1.2 Neuromorphic computing and mimicking nature

Many suggested solutions to these problems exist, including processing data and constructing the neural network. One field that is trying to combine the brain and artificial neural networks is neuromorphic computing. As mentioned, three differences must be addressed: energy efficiency, data reduction, and neuron specialisation. One of these methods is to specialise the neurons and bring them from digital to physical neurons. This would also help combine processor and memory, the von Neumann bottleneck problem. The problem, however, arises as to how this type of neuron is supposed to be constructed.

Biological neural systems do not use this digital 1 or 0 output but instead have an analogue range of possible signals. The AI models of today, deep neural networks, solve this problem by using 8-bit or even 4-bit weights. However, These weights need to be stored in the memory, which leads back to the von Neumann bottleneck. The neuromorphic computing solution uses processing-in-memory or computing-in-memory, where the weights are added to the physical components. This can be done by adding physical and variable resistance to the signal transmittance. This proposal makes it possible to move towards analogue data reduction and combine the memory and computing architecture, hopefully breaking past the von Neumann bottleneck [4].

In the EU, there are several projects for this specific field of research, and this thesis and project are written as part of one of them, the so-called InsectNeuroNano project. This project was funded and started in April 2020, with Lund University as the coordinator and Copenhagen University, Groningen University, and International Iberian Nanotechnology Laboratory as participants. There is also a partnership with the University of Edinburgh. The project aims "to develop innovative on-the-chip nanophotonic devices for integrated sensing and computation, inspired by the insect neural system"[6]. To achieve this, four lines of research will be combined:

- The neurobiological understanding of insects' autonomous navigation and the translation to circuit design

- Advanced III-V nanowire technology with light as the signal carrier for power efficiency
- Efficient photoswitching dyes with varying absorption spectrum for incorporating weight in the light signal
- Quantum computing circuit fabrication technology

With these four fields connected, the result is a highly interdisciplinary project in which each part takes inspiration and works with the others. The concept and goal of the project are to create a nanowire neuron circuit mimicking the insect's autonomous navigation, an idea further explored in Section 1.4.

1.3 Description of the neuron

The biological design of the neuron is not as crucial in this project as how well the physical model can mimic the BN. As early as 1943, researchers WS McCulloh and W Pitts constructed an artificial neuron model, which has been the standard since then [7].

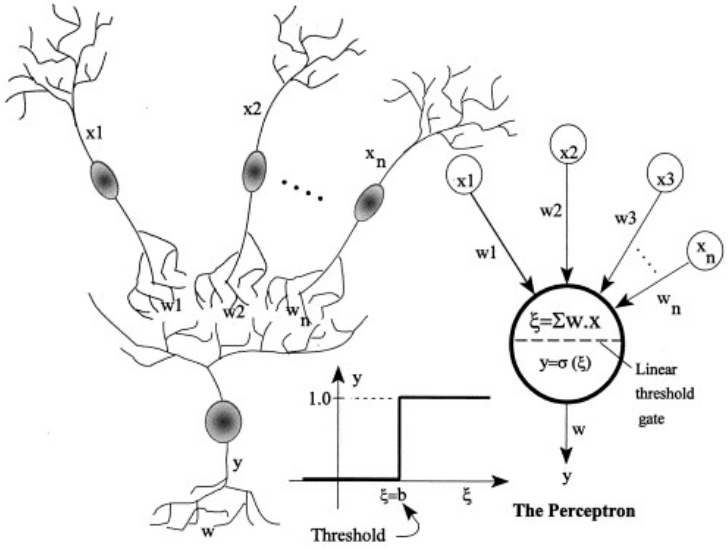

Figure 1: On the left, it shows the biological neuron compared to the artificial neuron on its left, from [7].

The artificial neuron [AN] is a mathematical model of its biological counterpart but captures the essential functions. Each neuron receives input from a set of n number of connected neurons, x_1 to x_n, Figure 1. The neuron then computes an input signal depending on the weight of each neuron connection denoted w1 to w_n in the figure. After the total input signal has been calculated, it either fires and sends out a signal or continues its rest depending on the result of the

activation function with the input signal as the variable. The activation function that is most used and the one closest to the BN is the sigmoid function. This is described by Equation 1

$$f(x) = \frac{1}{1 + e^{-x}} \tag{1}$$

where there is no output before some threshold value, the output quickly switches to a maximum value, after which there is no further increase. In the specific case of Figure 1, it shows the "Perceptron", which was a neuron model from 1958 [7].

From this model of the neuron, it is possible to extract some general properties defining it. In this case, it does not refer to the mathematical model as much as the biological one. These are

- Memory retention
- Excitation and Inhibition
- Sigmoid activation

The **Memory retention** in this case refers to both the memory of the individual neuron, which retains a short memory of input signals and the weight between the neurons. In the brain, many signals constantly travel throughout the neuron network. To utilise all the signals, each neuron has a short memory that remembers what inputs it has received. Over time, with many inputs, these signals can accumulate to activate the neuron. In the case of inter-neuron memory, it is the central component of how the neural network can solve problems and remember. The memory between neurons is represented by some weight, which modifies the output from one neuron to another. With a weight between neurons, the possibility of neural pathways that decode information is opened, allowing fluent memory encoding. This weight can be coupled to the frequency of signals between the two neurons, as in the case of biology. In that case, it will have some constant decay over time with an updating behaviour at each signal between the neurons.

The **Excitation and Inhibition** implementation is not present in the original model of the neuron but is essential for capturing the complexity of the biological neuron [BN]. In the brain, a neuron can receive two types of input signals. One is an excitatory input, leading to the output computation as seen in the model before. This is, however, not the only type of input a BN can receive. There is also the inhibitory input, which lowers the accumulated signal in the neuron, making it harder to fire. The inhibition creates more specialised neural pathways where each neuron fires less but is more specialised, avoiding neuron redundancy. This can be implemented by allowing the weights to have positive or negative values.

The activation function, or the **Sigmoid activation** in the case where the AN mimics the BN, is the condition for implementing weights. Without this, every input signal would fire the neuron, and no neural partways could be created. This activation function also stops many input signals to a neuron from overwhelming the neural network by saturating the output signal after activation.

After defining these parameters, it is possible to construct an AN, where a part of this AN has been implemented in the InsectNeuralNano project, of which this thesis is a part.

1.4 The neuron in its context

The idea behind the InsectNeuroNano project is to implement an AN model of an insect navigation system in the brain. The concept of how this will work is shown in Figure 2

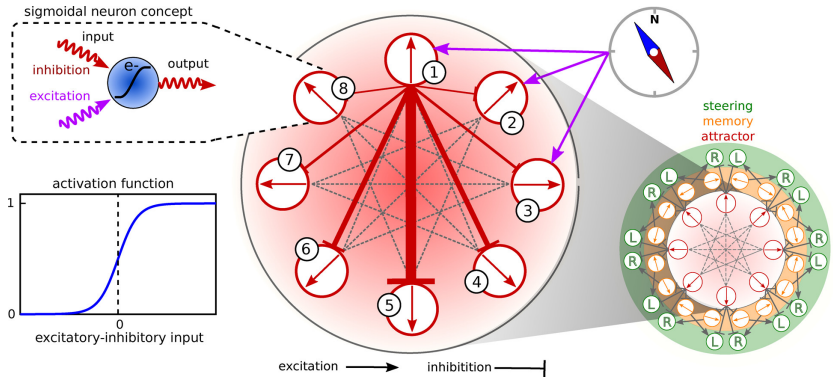

Figure 2: The Ring-attractor model of the most connected subcircuit (the figure in the lower right corner) in the model of the insect central complex. This part is responsible for encoding the insect's heading and computing the direction to fly towards when returning home. In the InsectNeuroNano project, the red attractor ring will be mainly modelled. Each of the eight neurons inhibits each other by a weight represented by the thickness of the line. In practice, this will be implemented by directing the light source such that the spread of the beam gives the weight distribution. Each neuron will have a compass direction connected to it, which computes the heading through the outer layers. From [8]

The novelty of the model is that it is through the geometry of the neuron placements that the correct weighted signals are transmitted. The navigation system model, the CX model, is straightforward and intuitive for such complex task management. The directional information is kept in the CX by keeping the activation of neurons on the attractor ring localised to the neurons that encode the desired direction through excitation and inhibition. However, This model does not describe the sensory part or how these signals contribute to the insect's navigation. This thesis focuses on the sigmoid neuron, upper left in Figure 2. The idea is to find an optoelectronic device that can receive inhibition and excitation light signals, convert them to electrons and perform a sigmoid evaluation, which can be transmitted as a light signal.

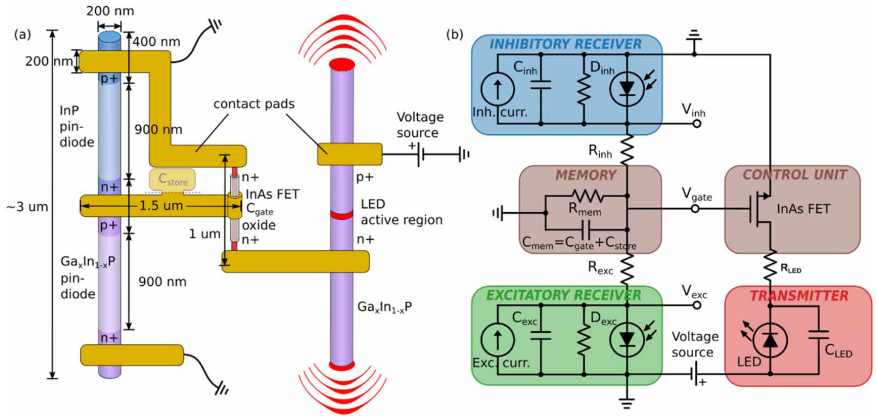

Figure 3: **(a)**, the nanowire AN will realise the CX model with one InP nanowire pin-diode for receiving exciting input signals and one for receiving inhibiting input signals. These are then connected to a gate that acts on the InAs nanowire, simulating the sigmoid activation function. The current through the InAs then leads further on to a $Ga_xIn_{1-x}P$ nanowire, which becomes the light source that sends out the output signal.**(b)** the circuit representation of the nanowire AN in (a). The bias V_{inh} and V_{exc} are not shown in (a) but represent the bias applied to each pin-diode. From [9]

In Figure 3.a, the implementation of the AN with III-V semiconducting nanowires (NWs) is shown. The whole NW neuron is shown with each part present: the excitatory receiver, the inhibitory receiver, the sigmoid activation function, the emitter and how they connect. In implementing the AN, the InsectNeuroNano project uses NWs due to several advantages compared to standard silicon devices. The NW can be manufactured with high control, mixing elements that target specific properties such as absorption peak and electron mobility. In the present work, III-V NW with high photon-electron conversion is used.

An additional part of the NW circuit is the memory on the gate. This memory didn't exist in the initial design but was later added, giving the setup much more stability since it could now accumulate signals better. This comes from the fact that the gate has a charging effect where the electrons after each signal do not immediately disappear, leading to a possible voltage buildup over time if many exciting signals reach the component. The novelty of this is that such an effect can also be observed in BN. This complete model has not yet been realised due to its complexity. As such, only a part of this neuron will be experimented on in this project. Figure 3.b, however, shows how complex this system is. There are two photodiodes: a field effect transistor and a light-emitting diode.

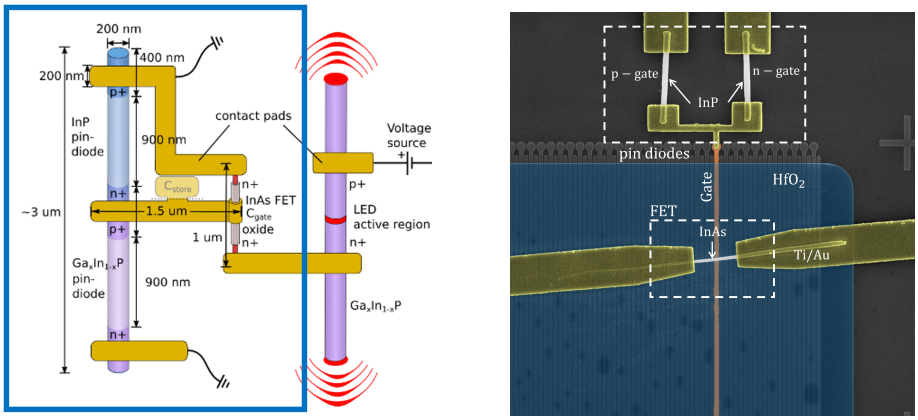

(a) (b)

Figure 4: **(a)**, the schematic of the neuron as shown in Figure 3 but where the blue box indicates which part of the neuron has been tested on in this project. **(b)**, the image shows how the different components are placed in the implementation of the part of AN, which is inside the blue box. The denotation n-gate and p-gate represent the inhibitory and excitatory receiver, respectively, and the name comes from which part of the NW is in contact with the metal leading to the gate.

Due to the InsectNeuroNano project not having finished the implementation of the NW neuron, only the part inside the blue box, see Figure 4a, is what is available and, thus, what has been tested in this project. One thing to note when comparing the figures is that there is no $Ga_xIn_{1-x}P$ in this implementation but instead two InP. One of the reasons for this is that only one laser can be used in measurements. The $Ga_xIn_{1-x}P$ and InP absorb with different efficiency at the same wavelength, which could lead to unreliable data if one laser was used for both. In Figure 4b, one of the devices that have been tested is shown. In this figure there are three parts of interest. The pin diodes are made up of the p-gate and the n-gate. The gate is connected to the pin diodes and goes under the InAs. The FET comprises an n-doped InAs with the gate being isolated from below by a layer of HfO_2.

Individual differences between the devices tested, devices 5 and 4, are insignificant and only affect the distance between the p-gate and n-gate. This difference is shown in Figure 5. The p and n-gate are pin-junctions connected with opposite polarity to the gate where the region connected to the gate determined its name, p or n-gate.

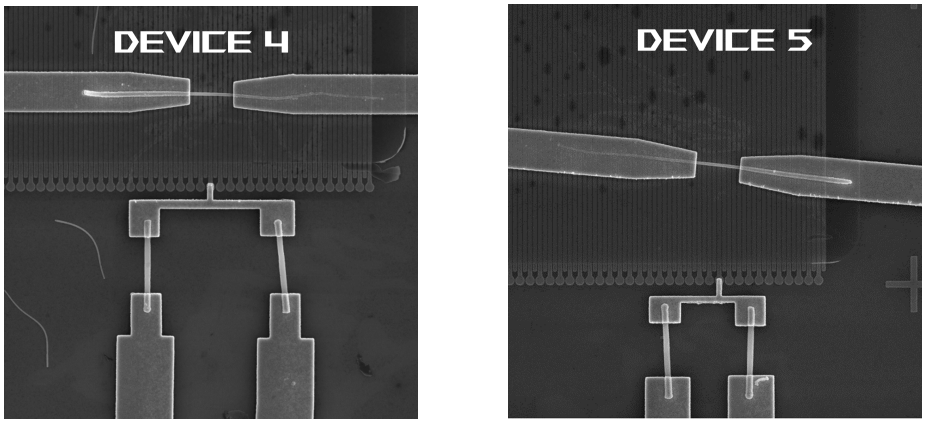

(a) (b)

Figure 5: **(a)** is device 4 is while **(b)** is device 5. The only significant difference between these two devices is that device 4 has a slightly large space between the p and n-gate.

For the neural network to be adequately implemented, it is essential to include memory in the weights (transmission strength between the neurons as described above) between the neurons. In the present case, this should function such that when a lot of light passes between two neurons, the transmission should increase and endure over time.

This memory is implemented by introducing a photoswitching dye between the neurons. The dye can switch between two states through photon excitation, where the ground state is non-transparent, and the excited state is transparent. A thermally activated back-reaction keeps the dye at a stable state with the signal frequency, where the stable state in darkness is the ground state. This will be further explained in the section 2.2.

This dye allows the AN to use photons as signal carriers, which are low energy and high speed compared to electrons. Initial measurements in the InsectNeuro-Nano project have shown that this dye has excellent potential, but a variance in how the dye is deposited has also been observed. This has motivated the research questions and experiments done in this thesis.

1.5 Subjects of investigation

How does illumination and gate bias influence the nanowire-based artificial neuron?

To test this, two things are deemed to be necessary. Firstly, a standardised set of measurements where the results from these can be compared between devices to determine the parameter space. Secondly, measurements that can probe further into the similarities of how the NW neuron compares to the BN will be called General measurements. The chosen set of standardised measurements

is discussed and presented in chapter 3.8.

How does the depositing of the photoswitching dye influence its properties?

To test this, a dye deposition method that is both systematic and repeatable has to be chosen. A list of parameters possibly affecting the deposition can then be gathered, and the number of them is constrained to be able to fit into the project's time frame. After measuring the finished samples, the data can be analysed and compared to theory to discover emerging patterns. The constraining of possible parameters is discussed in chapter 3.1 and builds on the results found in [10].

2 Theory

2.1 Semiconducting materials

The semiconducting material category describes a type of material between a conducting and an insulating material. These differences can be expressed in terms of the energy gap between their conducting and valence bands.

An insulating material has a large bandgap. This means that the electrons at room temperature do not have enough energy to get excited over the gap up to the conduction band.

A metal either has a partially filled conduction band or its conduction and valence bands overlap. Because of this, only a small amount of energy is needed to excite it so the current can flow.

A semiconductor's bandgap is smaller than the insulator's, so no electrons occupy any states in the conduction band at low temperatures. However, there is still a separation between conducting and valence bands. Some electrons are excited at room temperature, resulting in a moderate current. Three critical factors affect how semiconductors work and interact with light: the bandgap, the Fermi level, and whether it is a direct or indirect bandgap.

The bandgap is the semiconductors' most defining characteristic. It describes how much energy an electron needs to get excited from the valence to the conduction band, determining what light wavelengths can be absorbed or emitted. A critical measurement in the bandgap is the Fermi level, E_F, which measures the energy at which the probability of an electron occupying an energy state with energy E is 50 %.

This level can be shifted by something that's called doping. A doped semiconducting material has some atoms in the lattice changed for impurities in the form of atoms with one more or less electrons. Introducing these atoms opens up new sub-levels in the bandgap and can be categorized into two groups. When the atoms causing the sub-levels add electron vacancies, they lower the Fermi level, and the impurities are then called an acceptor, denoted with p. When the atoms add electrons, they push up the Fermi level and are called donors, denoted with n. At room temperature, the electrons in the donors are excited to the conduction band, while the electron vacancies in the acceptors are filled by

electrons from the valence band. If the semiconducting material is not doped, it is called an intrinsic semiconductor, denoted by i.

The type of bandgap the semiconductor has matter in its interaction with light. If the energy levels in a lattice are mapped out in momentum space, k-space, they form energy bands. These energy bands are highly complicated to describe but can be approximated by a parabola energy state distribution where the energy is inversely proportional to the mass. From this relation, a different mass comes out for the electron, which is called the effective mass of the electron. This effective mass depends on the material and is essential to describe how the electrical characteristics depend on the material. The holes left behind in the valence band by the electron can also be described as a type of quasi-electron with its separate effective mass.

When mapping the energy bands in space, they are combined so that the highest energy level in the valence band and the lowest energy level in the conductance band are the energy levels of primary interest. However, these two levels in the valence and conductance band do not need to occur at the same position in momentum space. When this happens, it is called that the semiconductor has an indirect bandgap. This separation in momentum means that the electrons have to absorb both a photon for the energy and a phonon for the momentum shift indicated in Figure 6. This makes the process slower and less likely. The processes for absorption and emission are similar, but only absorption is of interest in this project. When light interacts with the semiconductor, it needs to be absorbed by an electron. With no possible states between the valence and conduction bands, the lowest energy photon (also the highest wavelength) that can be absorbed is limited. Any light with insufficient energy cannot excite the electron over the whole energy band and cannot thus be absorbed.

The most common semiconductor is Silicon, which has an indirect bandgap, making it sub-optimal for photonics. In the case that the energy bands for a semiconductor align in momentum space, it is called direct bandgap and can easily absorb photons One such example is the compound semiconductor InP[11].

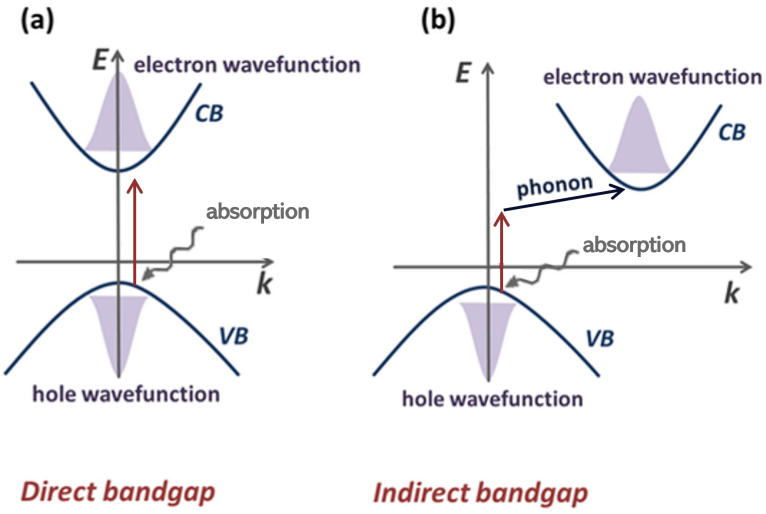

Figure 6: **(a)** is a direct bandgap where the electron only requires a photon to excite due to the VB peak and CB valley occupying the same position in k-space. **(b)** is an indirect bandgap where the electron requires a photon and phonon to excite due to the VB peak and CB valley not occupying the same position in k-space. Adopted from [12]

2.1.1 P-i-n junctions

The p—n junction is where one p-doped and one n-doped region are placed against each other. Since the p-doped region, also called the p region, has a surplus of positive charge carriers and few electrons, and the n-doped region, also called the n region, has a surplus of negative charge carriers and many electrons, an electric field is created between the two regions. In the middle between them, the p charges and the n charges cancel out, and a third type of region is created, the depletion region, over which the electric field is but with no excess electrons. The Fermi level of the p-n junction can be modelled and seen in Figure 7. Here W is the depletion region width, L_n the diffusion length of electrons in the p-region, L_p the diffusion length of holes in the n-region, E_C the conduction band, E_V the valence band, E_i is the intrinsic energy level and V_{bi} is the built-in potential between the p and n-region which comes from the doping of said region.

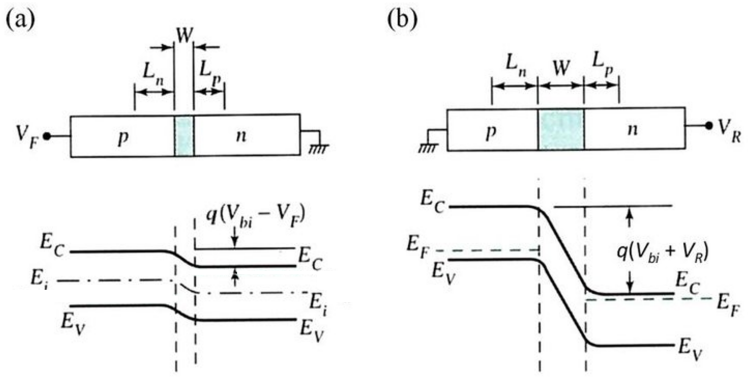

Figure 7: **(a)** is a forward-biased pn-junction which decreases the energy band shift from the doping. **(b)** is a reverse-biased pn-junction which increases the energy band shift from the doping. Adopted from [13]

A bias can then be applied to this device, adding another electric field to the regions. This bias can be applied in two ways: forward bias or reverse bias.

Forward bias: A pn-junction is forward biased when an applied voltage shifts the energy bands in the n-region upward and the energy bands in the p-region downward. Figure 7.a illustrates this by applying a positive voltage to the p-region while grounding the n-region. The energy band difference between the two regions due to doping is reduced by qV_F, evening out the energy levels and allowing more current to flow through the pn-junction.

Reverse bias: In the case that the voltage is related to V_F as $V_R \propto -V_F$ as in Figure 7.b then the pn-junction is reverse biased. The negative sign means that the energy band difference between the two regions is increased by qV_R instead. The energy barrier for charge carriers to move between the region is thus increased, and no current flows through the pn-junction.

These relations are expressed in the photo-diode equation, Equation 2.

$$I = I_s \left(e^{\frac{qV}{k_B T}} - 1 \right) - I_L \tag{2}$$

I_s is the leakage current, I_L is the current resulting from photon absorption, k_B is the Boltzmann constant, V is the applied bias, and T is the system's temperature. This equation describes the exponential increase in current with positive bias while negative bias saturates at I_s due to the reverse bias effect.

When light is absorbed, it can be in one of three regions: the p-region, the n-region or the depletion region. The photon is preferred to be absorbed in the depletion region to absorb the light as efficiently as possible since it is subject to the intrinsic electric field from doping. This electric field drives the electrons to the contact with the lowest potential, where they can be collected as current. Suppose any photons are absorbed outside of the depletion region. In that case, it lacks the electric field and must thus move to the depletion region

through diffusion, which is limited by the diffusion length, L_d. The diffusion length describes how long, on average, holes or electrons can diffuse before they recombine.

$$L_d = \sqrt{\frac{k_B T}{q} \mu_d \tau_d} \tag{3}$$

where τ_d is the specific lifetime, d is the doping type, and μ_d is the electron mobility. An intrinsic region can be put in between the two doped regions. With a pin-junction, the intrinsic region will effectively extend the depletion region with a constant, though weaker, electric field. To achieve good photon-to-electron conversion, there are thus three main things that can be considered: either the depletion region or the electron/hole mobility must be large or the specific lifetime is long [14]. Another possibility used in this implementation of the AN is to insert an intrinsic region between the p and n regions to extend the depletion region.

The two InPs in Figure 4b are pin diodes, and each of them can implement either the excitatory or inhibitory effects. The absorption of a photon increases the holes in the p-region and the electrons in the n-region.

The n-gate can implement the inhibitory effect since the n-region of this pin diode is connected to the gate. The voltage that results from the increase in electrons is negative and is applied over the gate, thus lowering the gate voltage; more about this in the next section. For the p-gate, holes are used instead to increase the gate voltage.

Assuming that only the n or p-gate is absorbing at a time, the voltage generated is the open-circuit voltage, V_{OC}, given by setting $I = 0$ in Equation 2.

$$V_{OC} = \frac{k_B T}{q} * \ln\left(\frac{I_L}{I_S} + 1\right) \tag{4}$$

If both pin diodes absorb the same amount of light, then the voltage supplied by the p-gate and the voltage supplied by the n-gate will cancel out in the gate. Instead, a current will be registered through the pin diode region.

2.1.2 Field effect transistors

The field effect transistor [FET] is one of the most used approaches to controlling currents in semiconductor devices. It applies an electric field to a control region, usually through an isolated metal contact, allowing control of the current through the region. Two important concepts here are the minority and majority charge carriers, where charge carriers refer to what makes up the current in that region, holes or electrons. The minority charge carriers are the least common charge carriers in that region; for a n-region, it would be holes. While the majority of charge carriers are the most common charge carriers in that region, for an n-region, it would be electrons.

Most of the time, a FET is used with some diode with differently doped regions interacting, but in this project, the InAs used for conducting electrons were intrinsic.

In a diode, the electric field shifts the energy bands in the control region such that a channel for minority charge carriers opens. The diode is then made such that these minority charge carriers in the control region are the majority charge carriers in the regions on each side of the control region. This means that the channel's size or the charge carriers available in the two other regions limit the current. If only the electric field changes, the expected IV shape is a sigmoid-shaped curve. The energy distribution of electrons gives rise to the initial exponential response of the current. At some point, however, the energy band has been shifted so much that the available charge carriers limit the current, and saturation occurs. If the external bias is sufficiently large, V_F in Figure 7 creates a pinch-off. The external bias is then strong enough to cancel out the electric field in the channel closest to the bias. So far, the current has been increasing as described in Equation 2 but now reaches a saturation where, in theory, the current is constant with increasing bias.

It is slightly different for the InAs compared to a diode. Because no doped regions are present in the InAs, the majority charge carriers are used as current. Instead of opening a channel, the electric field applied on the InAs shifts the energy bands of the whole InAs, allowing more or less current to flow. For the InAs, if only the electric field changes, it will give rise to the same response as mentioned, which is an expected sigmoid behaviour.

2.1.3 III-V Nanowires

Si is the most used semiconductor but is surpassed in physical properties such as electron mobility and photon-electron conversion by combining materials in the III and V atomic groups, such as Ga, In, As, etc. One of the drawbacks of combining different elements in III-V semiconductor devices is that they often have different lattice spacing, meaning that, when forcing them to be part of the same uniform crystal structure, deformities emerge. There are, however, some III-V combinations that aren't true due to similar lattice spacing. These deformities can, in some capacity, be tolerated or patched up but limit the scaling and effectiveness of the device. One solution is shifting it from a 3-dimensional device to a semi-1-dimensional device with a sizeable height-to-width ratio. This cylindrical device is, fittingly, called a nanowire [NW] with a typical height of around a few μm and a roughly 100 nm diameter. The 1-dimensional structure allows some of the tension in the lattice spacing mismatch to relax by slightly altering the diameter of the NW.

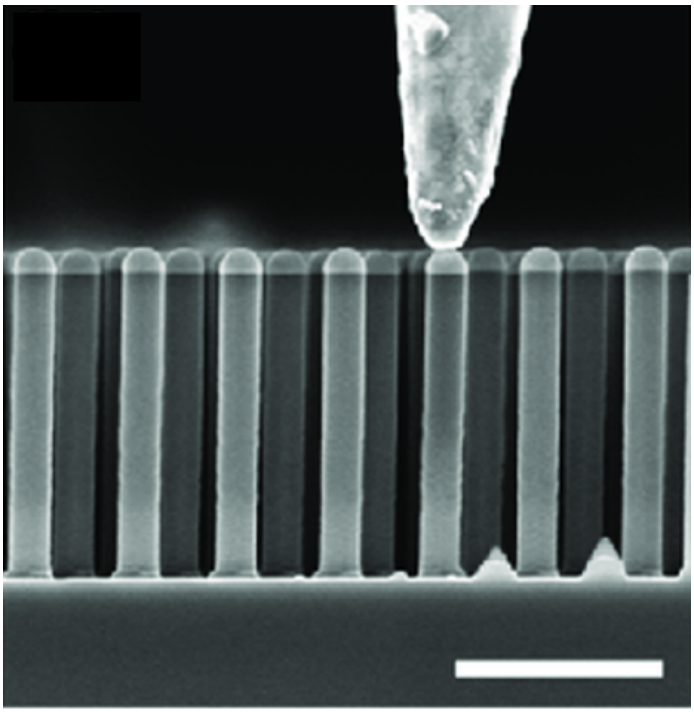

Figure 8: A cross-section SEM image of a nanowire array where the white ruler is 1 μm. Adopted from [15]

Due to their thin diameter and more flexibility with material mixing, the NW has shown great promise in computer science, solar cells, medicine, communication, and so on. The most significant advantage of the NW over standard FETs is that the electric field can be much better controlled with an all-around gate that, at the same time, can also pacify the surface traps. Other advantages of the NW include freedom in growing them and high electron mobility [16]. In ordinary FETs, the gate covers only a small part of the device, and leakage currents are unavoidable. In an all-around gate, the field has a better reach into the substrate and covers much more of the device, making it more responsive and avoiding such things as leakage currents[17]. These advantages make the NWs attractive in highly specialised components such as in the mentioned NW neuron.

One of the problems with NWs is that they have a lot of surface trap states, which makes them exhibit unwanted behaviour, such as fading memory effects from a few to a few tenths of seconds. These surface traps have poor light emission and detection efficiency since they will capture excited electrons[18].

The NW used in this project for the NW neuron is InAs and InP. InAs have far superior electron mobility than Si, motivating its use for the conduction of electrons. InAs is also intrinsically n-doped[19], which makes ohmic contacts easy to make and means that the majority charge carriers are electrons. As for InP, it does not have as good electron mobility as InAs but has a better native oxide,

thus fewer surface trap problems, meaning far better photoelectric properties. Its bandgap limits its interaction with light with a wavelength below $\approx$ 920 nm, though not as much as InAs, whose bandgap absorbers at $\approx$ 3500 nm. In this project, the preferred wavelength is around 660 nm, and the greater the bandgap deviates from this, the worse the absorption is. This deviation is not optimal but not problematic for InP, and InAs should preferably not interact with light.

2.2 Molecular memory systems

To describe the molecular memory systems studied, it is good to introduce light-molecular interactions briefly. When a photon interacts with a medium and is absorbed, the absorbing molecule enters an excited electron state. This state is unstable for most mediums, and a decay process is quickly initiated, which either goes through a radiative or non-radiative decay. Radiative decay is the remittance of a photon by the molecule by the electron as it jumps from its excited state back to the ground state. Non-radiative decay, on the other hand, does not involve any photons, and the decay can use different paths. These can include vibrational modes or similar energy transfer inside the crystal [20].

The Beer-Lambert Law can model the intensity of the incoming and outgoing light from the molecule. If there is a beam of light with a given intensity, let's denote it I_0, then the outgoing intensity, I, from the medium can be described by Equation 5.

$$I(\lambda) = I_0 * 10^{-A(\lambda)} = I_0 * T(\lambda) = I_0 * 10^{-\epsilon(\lambda)lc} \tag{5}$$

$A(\lambda)$ is the absorption of the wavelength at which the outgoing intensity is measured, and $T(\lambda)$ is the transmission at that same wavelength. The last relation where $\epsilon(\lambda)$ is introduced describes the material-specific effect on the intensity where $\epsilon(\lambda)$ is the molar absorption coefficient measured in L (litre) * $\text{mol}^{-1} * \text{cm}^{-1}$, l is the thickness of the absorbing medium measured in cm and c is the concentration of the material measured in mol * L^{-1} [20].

2.2.1 Donar-Acceptor Stenhouse Adduct dyes

Among the molecules that interact strongly with light, the subcategory of photoswitching dyes can be either irreversibly or reversibly bleached. If irreversibly bleached, the dye enters a state from which it cannot return to its original ground state, while reversible bleaching can return to the ground state. Donar-Acceptor Stenhouse Adduct [DASA] dyes are a particular type of photoswitching dye that can switch their molecular structure with photon absorption.

Shown in Figure 9.a is the photoswitching nature of the DASA dye. The ground state [GS] absorbs a photon in the far red or near infra-red [NIR] range with energy E = hv and can thus go from an open to a closed metastable [M] state, which now is colourless. This process is reversible through Δ, which denotes a thermally-activated decay in the figure. Figure 9.b shows how the GS absorption spectrum changes over time to the M absorption spectrum when under illumination. Here, it is showcased with the dye dissolved in Toluene.

Figure 9.c is a more in-depth sketch of how the states interchange in Figure 9.a. An opaque ground state absorbs a photon and enters an excited state from which it can decay back to the GS or to the transparent M state. From this M state, it then has a thermally activated decay back to the GS[21].

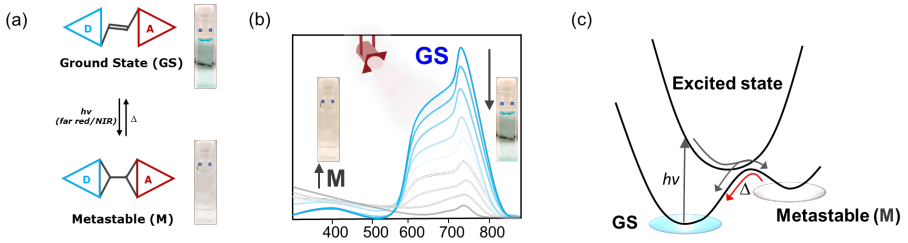

Figure 9: **(a)** showcases how the GS and the M state interchange. **(b)**, displayed is the spectrum changes over time when illuminated. **(c)**, this is a more fleshed-out description of what happens in (a). Figures credited to Abbey M. Philip

In this project, a specific type of DASA was used, displayed in Figure 10. The red and blue ends of the DASA molecule are changeable, which creates some variance in how they can be tuned for decay time and absorption peak. Figure 10a shows the possibility of having several different DASA dyes with similar or different absorption peaks.

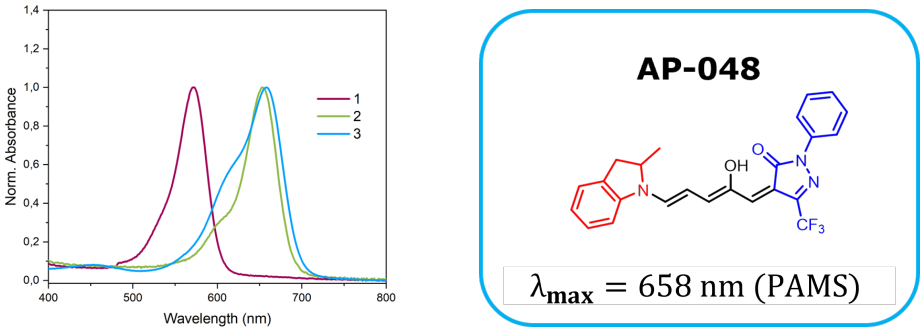

(a) (b)

Figure 10: **(a)** showcases three different DASA dyes where AP-048 is the blue line, or the one called 3. **(b)** displays the AP-048 molecule with absorption peak when mixed in Toluene and PAMS. Figures credited to Abbey M. Philip

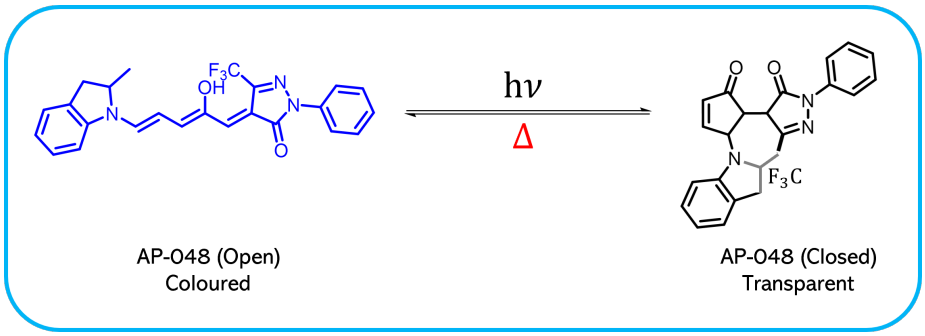

Figure 11: A illustration of how the dye goes from an open, coloured GS to a closed, transparent M state by light absorption and then decays back to the GS by thermal back-reaction. Figures credited to Abbey M. Philip

2.2.2 DASA-kinetics Model

To describe the DASA kinetics, the total concentration described in Equation 5 as c, from now on denoted c_{tot}, must be split into two parts. In this project, these parts will be called the ground state [GS] molecule concentration, c_{GS}, and the metastable [M] molecule concentration, c_M. The ground state molecules can absorb photons and are in the open GS, while the metastable molecules are in the closed M state.

$$c_{GS} = c_{tot} - c_M \tag{6}$$

Since only the GS molecules can absorb light, it is possible to rewrite Equation 5 such that the intensity is expressed as a function of GS or M molecules.

$$I = I_0 * 10^{-\epsilon l(c_{GS})} = I_0 * 10^{-\epsilon l(c_{tot} - c_M)} \tag{7}$$

This now describes a steady state. The time-dependent expression must also include some description of how the absorbed photons respond to the excitation of molecules as well as a possibly changing I_0. The time-dependent absorption, $A(t)$, can be found if the incident intensity I_0 can be known from the measurement instruments. With only c_{GS} absorbing, the fraction of the I_0 absorbed is simply the photons not transmitted. This might not be the entire picture, as the GS molecules do not absorb all these photons, but this is a good enough approximation.

$$A(t) = I_0(t) * (1 - T) \tag{8}$$

Assuming that not all photons absorbed excite a molecule, an absorption constant is formulated, Φ_{GS}, that describes the efficiency of photon excitation for GS molecules. With these relations, a new term called the bleaching term is introduced, which refers to how quickly M molecules are bleached. Thus, the bleaching term, B, of the M molecules is

$$B = I_0 * \Phi_{GS} * (1 - T) \tag{9}$$

The expression for the transmission is now substituted for the expression in Equation 7, $T = 10^{el(c_{tot}-c_M)}$, with the added assumption that the population c_M and c_{GS} will change over time.

$$B = I_0 * \Phi_{GS} * \left(1 - 10^{-\epsilon l(c_{tot}-c_M(t))}\right) \tag{10}$$

In the same way, a decay term can be formulated that describes how quickly the M molecules decay or return to their GS. The decay term, D, of the M molecules is thus

$$D = -k * c_M(t) \tag{11}$$

where D is the first-order back-reaction, k is the rate coefficient and is related to the half-life of the thermal decay by

$$t_{1/2} = \frac{log_{10}(2)}{k} \tag{12}$$

Thus, the total change over time for the concentration of M molecules, c_M, is the sum of the bleaching and decay terms

$$\frac{dc_M(t)}{dt} = B + D \tag{13}$$

Substituting the equations for B and D gives the final result of

$$\frac{dc_M(t)}{dt} = I_0 * \Phi_{GS} * \left(1 - 10^{-\epsilon l(c_{tot}-c_M(t))}\right) - k * c_M(t) \tag{14}$$

This final result can be solved numerically and used when fitting the photoswitching dye transmission spectrum[10][22].

These kinetics are further modified by the thin film polymer mixed with the dye used in the project, PAMS, Poly(α-methylstyrene) and how they are deposited. This includes heating, the deposition method, and an unknown number of other parameters.

3 Method

Data gathering and extraction can be divided into sample preparation, photoswitching dye measurement, and NW devices.

The dye was provided by Abbey Meprathu Philip and Bo Wegge Laursen from the University of Copenhagen and was called AP-048. AP-048 has an absorption maximum at $\lambda_{max} = 652$ nm, and the half-life has previously been measured to be $t_{1/2} = 160$ s in PAMS by Abbey M. Philip.

For the NW sample, there was cooperation between Lund University and Copenhagen University, where Joachim Sestoft was responsible for the final product.

3.1 Dye preparation

The dye mentioned in Figure 10 was deposited on sapphire samples of 1cmx1cm. The dye in its pure solid form, provided by Abbey Philip in Copenhagen, was dissolved in a 1:9 Toluene: Dichloromethane solution with the previously mentioned PAMS at 15% wt./wt, all done in the Division of Chemical Physics by Thomas. K Jensen. Previously, in [10], the dye had been drop-casted and spin-coated, and although drop-casting had provided good results, spin-coating was chosen in this project. This had the research questions as motivation since the goal was a more systematic way to deposit the dye with consistent results.

Drop-casting involves simply dropping the dye on top of the sample and letting it dry, which results in a non-uniform and non-predictable thickness.

Spin-coating, on the other hand, works by putting the sample on top of a pillar which is free to rotate. The spin-coating program begins to rotate the sample slowly so that the dye can be drop-casted on top. A few seconds in, enough time to drop-cast the dye, the pillar accelerates to a chosen rotation per minute [rpm]. This high-speed rotation means that the dye will, through centripetal force, be forced out from the sample centre. With most of the dye being thrown off the sample, what is left behind is a smooth and even surface.

Due to time and instrument limitations, certain constraints had to be placed on the research questions. The goal was to minimise the difference in significant parameters between each batch to create a more standardised method of dye preparation. In previous measurements on the dye, AP-048, drop-casting has been used due to the good results, but that is substituted for spin-coating for consistency.

The relevant parameters for the dye preparation and deposition are the following:

- Annealing
- Atmosphere when annealing
- Temperature when annealing
- Spin-coating speed (connected to the thickness)
- Dye concentration
- Sapphire surface contamination
- Age of dye solution
-

Among these, a few parameters believed to have the most significant effect were chosen. Here, the parameters needed to be easy to control in the experiment and have a clear way to be measured. Below are the five parameters mentioned.

- Annealing

- Atmosphere when annealing
- Temperature when annealing
- Spin-coating speed (connected to the thickness)
- Dye concentration

However, these parameters could not be tested since the number of samples would become between 2^5 and 4^5. Here, time came into the picture, and the parameters had to be limited to annealing, the atmosphere, and the spin-coating rpm. The dye concentration was limited to 5mM (1% wt./wt) using Thomas K. Jensen's thesis results as motivation [10]. The temperature was limited to either no annealing, i.e. no temperature, or 50° Celsius by the advice of Abbey M. Philip. The available instrumentation for annealing was a Rapid Thermal Processor 1200, which gave the option of annealing with atmosphere 100% N_2 or 5%H_2 and 95%N_2. The option with atmosphere N_2 was chosen, and 5%H_2/95%N_2 was discarded due to their similarities. The slight change in the atmosphere could give rise to changes. Still, the difference between no annealing and annealing with N_2 already presents a sizeable variable difference. The variance from the 5%H_2/95%N_2 option is considered irrelevant compared to the variability between batches.

Finally, a set of independent parameters was created, with 8 different samples shown in Table 1.

Name	Variations
Spin-coating	1500rpm ,2500rpm ,4500rpm ,6000rpm
Atmosphere	N_2
Annealing	No annealing or 50°
Dye concentration	5mM (1% wt./wt)

Table 1: The final set of independent parameters that was chosen to test in this thesis

3.2 Solar simulator G2V Pico

The solar simulator G2V pico is a setup designed for the characterisation of photovoltaic devices. Many calibrated LEDs can be individually controlled and set to the desired power, providing numerous illumination spectrums. Only the 633-711 nm LED was operated in this work since it best overlaps with the spectral absorption range of the DASA dye used, AP-048; see Figure 10.

At first, the measurements used were 7 minutes of exposure with 500 LED power and a total irradiance of 1.2 mW/cm^2 as was the setup used in Thomas K. Jensen's master's thesis,[10]. This worked for 1500 with no heating, but a pattern quickly emerged that indicated that the exposure was not enough, and since the second bath, annealed with N_2 atmosphere, was thicker, a longer exposure time was chosen. Thus, every measurement except the 1500 no heating used 15 minutes of exposure instead.

There were two extra measurements, which used their own setup. The changes, 500 to 1000 LED Power and 15 to 30 minutes of exposure were done to test how these parameters changed the transmission over time for the photoswitching dye. With a 1000 LED Power setup, the solar simulator had a power of 2.4 mW/cm^2.

The Solar simulator is used to illuminate the sample such that an initial population of c_{GS} is excited to c_M. When this program is run on the solar simulator, it is moved to another setup. The transmission is measured there while the c_M decay back to c_{GS}.

3.3 Light transmission through dye

The transmission was measured using an integrating sphere in a Bentham PVE300 over 400 to 1100 nm. This works by letting light be transmitted through the sample into a closed sphere, the integrating sphere. A detector collects the light from different parts of the spheres inside, and the total amount of transmitted light can be calculated.

One important thing to note is that the aperture, which controls how large an area of the sample is exposed, was changed during the project. At first, a small aperture below 0.74 mm was used, but it was later switched to a 1.5 mm aperture due to the bad signal-to-noise ratio. The exact dimensions of the first aperture were also not known, only that it was below 0.74 mm since this aperture was modified.

In the Bentham setup, a few measurement artifacts shape the transmission profile, which motivates a normalisation of all the data to a standard transmission measurement. Two measurements were thus done, one without any sample and one with only a blank sapphire sample, as seen in Figure 12. The normalisation was then chosen against the blank sapphire sample since only the effect of the photoswitching dye on the transmission profile was of interest.

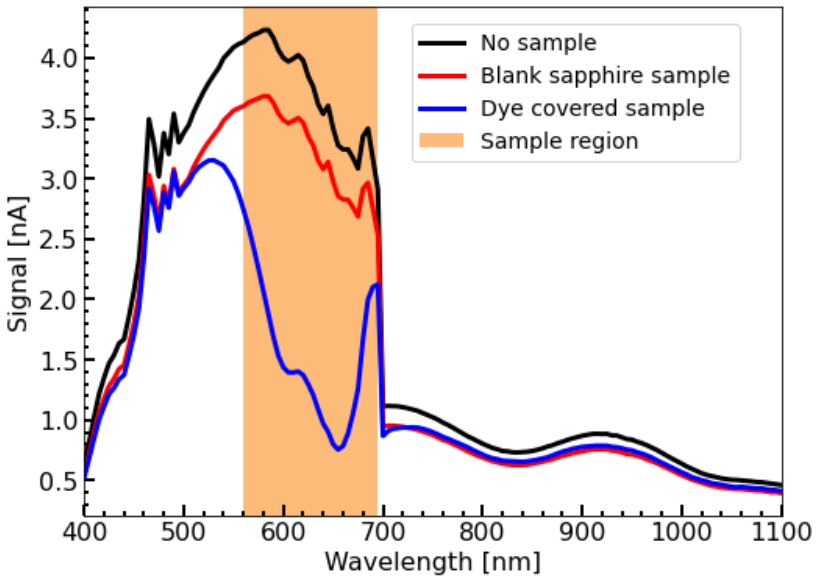

Figure 12: The difference between the transmission of no sample, the blank sapphire sample and a dye-covered sample. The orange region is the spectral range at which the dye absorbs strongest. The data collected was limited to this range when looking at transmission over time.

Since the dyes do not absorb at all wavelengths, only a part of the range was chosen where the transmission spectrum was maximally affected. Figure 12 highlights the wavelengths for which the data was used. This range does not cover the whole range for which the photoswitching dye absorbs, but it is where it absorbs most strongly. A limited range helped to avoid accumulating noise in the regions where the signal-to-noise ratio was worse.

The following assumptions were made when modelling this project's transmission change. After having illuminated the sample, the M population, c_M, is a non-negligible fraction of the total population, c_{tot}. The intensity in the transmission measurement will not be zero but will be assumed to be small enough such that $D \gg C$. With these assumptions, Equation 14 can be simplified

$$\frac{dc_M(t)}{dt} = -k * c_M(t) \tag{15}$$

Which is easily solved and gives the expression used to fit the decay of transmission data.

$$c_M(t) = e^{-kt} \tag{16}$$

3.4 DektakXT profilometer

A Bruker DektakXT profilometer, with a maximum sub-nm resolution, was used to measure the thickness of samples. It places a probe on the sample's surface and sweeps it a certain distance while recording the variation in height. The thickness can be extracted if the measurement starts at a point with no dye, such as a scratched edge. However, this is difficult if the sample is uneven and only an average thickness can be calculated.

3.5 Optical beam-induced current

The Optical beam-induced current [OBIC] used to categorise the optoelectronic response of the NW devices is the same as described in Thomas. K Jensen's master's thesis [10]. The OBIC is a spatially resolved measurement technique that runs on a modified Unisuko SPM setup where the STM probe wasn't used.

The operating principle is that a light beam from the laser diode in Figure 13 can be moved over an area. While moving the beam, the currents in Figure 15 are recorded as the pixel value at the beam's position when recording the current. After the beam has moved over the whole area, each current will be saved as a separate heatmap where every pixel corresponds to the recorded I_{InP} or I_{InAs} when the beam is at that position. The speed of the beam and the size of each pixel can be changed, but in this project, they were kept constant with maximum scan area.

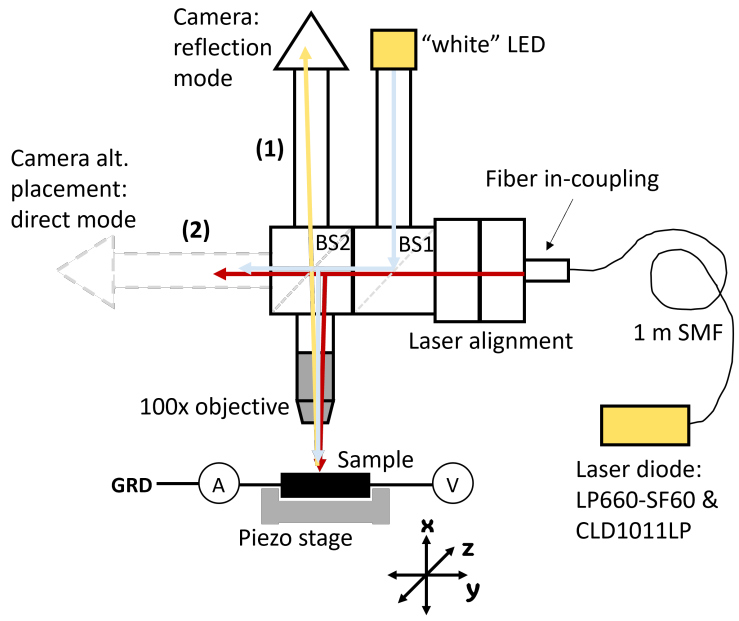

Figure 13: The Unisuko setup with camera, laser diode, white LED, sample and piezo stage [10]

A monochrome CMOS digital camera, Thorlabs DCC1545M-GL, was used to image and navigate the sample in the Unisuko setup.

A white-light LED, Thorlabs MNWHL4, was used when placing and focusing the camera on the sample together with a Thorlabs LP660-SF60 laser diode with a central wavelength of 660 nm for characterisation. A Thorlabs CLD1011-LP laser diode driver controls the laser diode. A Single-mode fibre then guides the light to a laser alignment where angular and translational alignment relative to other optical components is possible. The beam continues and passes through two 50/50 beam splitters where the second one, BS2 in Figure 13, guides part of the beam down to the sample while the other part is guided to position (2), which is an alternative camera placement not used in this project.

The piezo stage and the beam spot size limit the spatial resolution in this setup. The piezo stage moved by piezoelectric actuators has a sub-Å, 10^{-10}m, resolution in all three dimensions, x, y and z. On the other hand, the beam spot size has roughly 1 μm diameter, which is the limiting factor in the OBIC scans.

The laser diode and the piezo stage can be controlled remotely on a computer, where the laser diode control was handled in Python.

Throughout this project, a 100X objective lens, Olympus LMPLFLN100X, NA= 0.8, was used [10].

The circuit connected to the sample has been slightly adjusted from the one presented in [10] since the device described in section 1.4 is more complex.

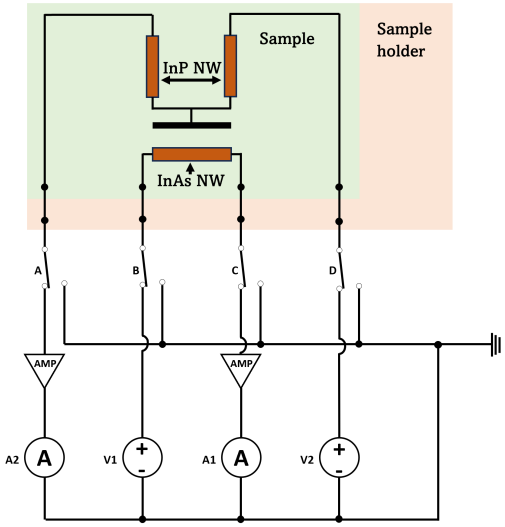

Figure 14: A schematic of the Unisuko setup. In this setup, the InAs have been connected to contact B using the Unisukos built-in ammeter and to contact C using the Unisukos voltage source or the lock-in amplifier. The Unisuko built-in setup is used for the OBIC scans, while all other measurements trade the voltage source for the lock-in amplifier. Two InP NW are connected to a gate under the InAs and to contacts A and D, which are part of the built-in Unisuko setup. AMP is the external Femto DLPCA-200 amplifier.

The sample holder was a stage with four isolated conducting islands on which the sample rested. These were then connected to a sample holder on which two sets of bias can be applied, and with the help of external Femto DLPCA-200 amplifiers, two corresponding currents can be read out.

3.6 Circuit description

In the OBIC, there are four parameters in each measurement. V_{InP} is the bias over the two InP's NW, and since the InPs are connected to the gate, this bias is also the bias gating the InAs. I_{InP} is the current through the InPs, and since no current should flow from the InPs to the InAs, this current is isolated from the InAs by a layer HfO_2. V_{InAs} which is the bias over the InAs and the I_{InAs} which is current through the InAs. In Figure 15, there are two blue squares, a light blue square and a dark blue one; these two positions will be referred to during this project.

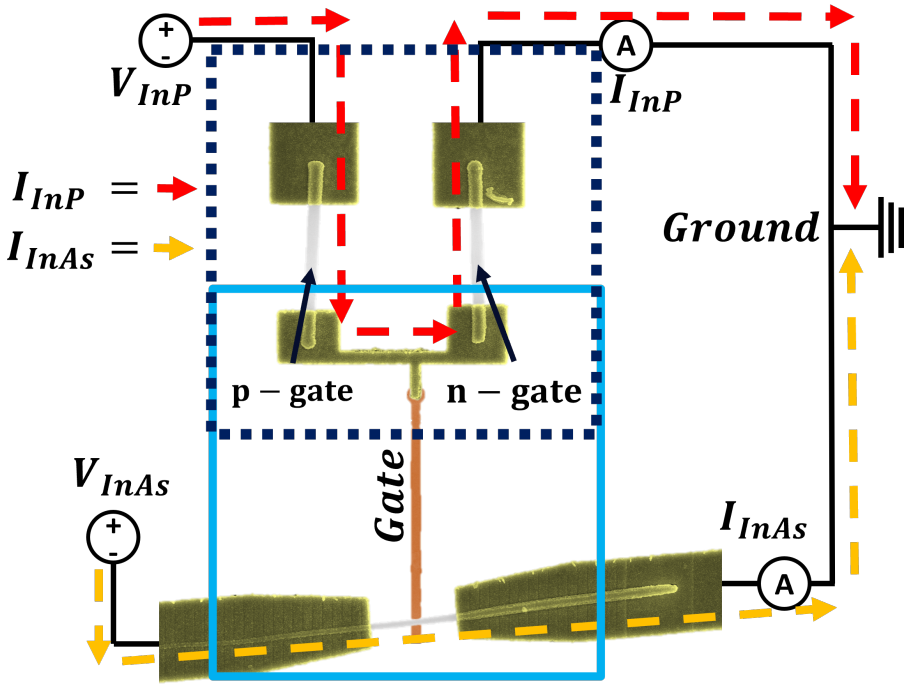

Figure 15: A circuit description of the NW neuron as implemented in the project. This figure refers to all references to readout current, biasing voltage, and OBIC scan window position going forward. The p-gate is the excitatory receiver, and the n-gate is the inhibitory receiver.

The whole system has a common ground, and I_{InP} and I_{InAs} can be measured in parallel.

When running an OBIC scan, both currents are measured while the beam sweeps in a zig-zag pattern over the small light-blue or dark-blue region. At each point, the currents are measured and registered as a value in a matrix represented by a heat plot. Since the beam optical power is constant throughout the measurement, the result will be a 2D spatially resolved heatmap of photo-induced current for the I_{InP} and a mapping of the gate response to this current for the I_{InAs}, where each pixel measures how the current responds to the beam at that point. This is not entirely true for the case of the I_{InAs} since the InAs also have a photo response, though smaller than InP.

Since the two InPs have switched polarity connected to the gate, I_{InP} sees the p and n-gate as series connected such that the pin-junctions have the same bias polarity. In conclusion, both of the NWs are either forward or reverse-biased.

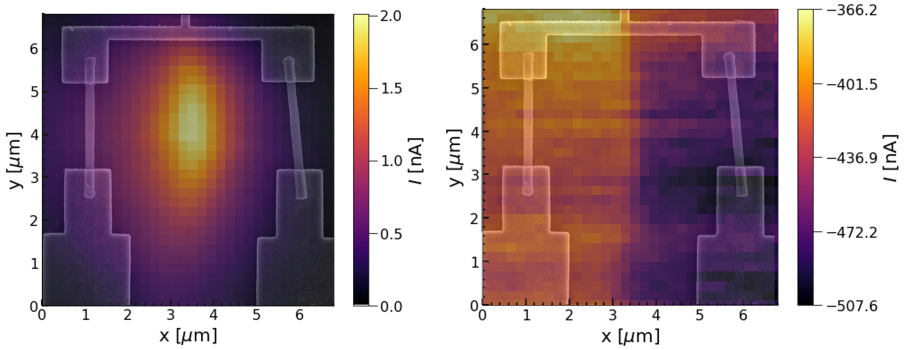

(a) I_{InP} (b) I_{InAs}

Figure 16: OBIC scan on device 4 on sample PT9 where **(a)** shows the I_{InP} response and **(b)** shows the I_{InAs} response. The scan was measured for $V_{InP} = 0$ and $V_{InAs} = 20$ mV and an optical power of roughly 3.76 μW. The OBIC scan over the dark blue dotted region, see Figure 15

An example of an OBIC scan with the NW device overlaid the scan can be seen in Figure 16. Only a small bias, V_{InAs}, have been applied within the IV region where the current is Ohmic, linear increase with bias. The InAs NW is homogeneously n-doped and responds as a resistor at low voltages. Measurements with no light have shown a small current at 0 V. Due to the difficulties in setting the bias to exactly 0 V, the conductance (slope of I(V)) was measured.

The maximum current in Figure 16a is recorded when illuminating between the two InP nanowires because, with the configuration of the p-i-n followed in series by an n-i-p wire, the total current through the circuit will be determined by the minimum of the currents through the two wires. This current is, in turn, affected by the illumination of the individual wires. Thus, when both wires are affected maximally simultaneously (when the light is in the middle), the current through the complete circuit will be maximal.

In Figure 16b, the current depends on which side is illuminating since one side of InP implements the inhibition while the other implements the excitation. The n-gate implements the inhibition by generating elections to the gate as photoresponse, while the p-gate implements the excitation by generating holes.

3.7 Conductance

Halfway through the project, the Unisuko setup previously used was expanded with a Stanford Research Systems SR830 Lock-In Amplifier. A Lock-In Amplifier works by sending in a signal with a known frequency, preferably in a low noise frequency range. It can then measure even a very weak output signal in a noisy environment by focusing on the device response in the known frequency response. Since the change in voltage is measured, it is not crucial to set it to exactly zero. This was used to get a better signal output with a Python environment called

QCoDeS, which enabled high control over the device and easy and simultaneous readout of current and conductance [23]. The conductance, $G = 1/R$, is measured in Simens [S] and was used for several measurements. The conductance was only measured on the InAs.

This enabled a much easier way to access the devices' differential conductance, which could now be measured simultaneously as the current. It does this by sweeping the bias in a small range around 0 and measuring the current, assuming that the InAs have a linear relation between current and bias in this range.

3.8 Standardised measurements

One major change when transitioning between the measurement of device 4 and device 5 was the introduction of the lock-in amplifier. At the same time, enough data was gathered for a standardised set of measurements to be created. These measurements became Conductance, Sigmoid curve and OBIC scan.

The **Conductance** is measured using the lock-in amplifier with a number of data points over a variable time. This time may vary depending on the desired precision and the noise present. The Conductance is then taken to be the average value of these data points.

It is crucial to test this even before continuing with the rest of the experiments. Conductance measures the device's electrical performance and reveals how well it compares to the desired performance.

The **Sigmoid curve** can be measured in two different ways, either with a linearly increasing optical power with beam focus on top of the NW or with the beam off-centre from the NW. A few experiments must be conducted to find the optical power at which activation occurs before the Sigmoid curve can be measured. This is especially true when the beam is off-centre since the distance between beam focus and NW determines the optical power at which the Sigmoid curve appears. The interest in the Sigmoid curve comes from the necessity of this function to implement the neural network.

The **OBIC scan** is the final standard measurement since it demonstrates the essential inhibitory and excitatory of the NW neuron. The pixeled map that emerges maps out how the different parts of the device respond to the beam interaction. This is important for discovering irregularities and differences between device designs and responses. Figure 16a shows an example of this inhibitory and excitatory measurement, where one InP increase the I_{InAs} while the other decreases it. Between them, there is a sharp line which defines the inhibitory versus excitatory regime.

4 Result and Discussion

In this section, the different results obtained during this master's thesis will be presented. First, the results from measurements on NW neurons will be presented; see section 4.1 and 4.2. After which the result from measurements on the DASA dye will be presented in section 4.3.

4.1 Optoelectronic measurements on a NW neuron

All three standardised measurements were completed on device 5 on sample PT9; see Figure 5b. Measurements were done on the other devices, such as devices 4 and 3, but they broke quickly, and standardised measurements could not be completed. As for the data set on device 5, since it survived for the longest time, it enabled further measurements, which can be found under Section 4.2.

4.1.1 Conductance

When it comes to the conductivity measured in darkness, there was a high variance depending on the time of measurement, as seen below in table 2

Time of measurement	**Conductance** [μS]
Beginning of measurement	2.75
End of measurement	1.90
Overnight	2.27
Average	2.3

Table 2: The conductance value through the InAs NW at different times. Note that no wait was included between measurement and the "End of measurement" to avoid memory effects in the NW. The measurement lasted around 2 hours.

The results in table 2 are not uncommon since the currents running through the NW and the atmosphere in the measurement room can effect the surface and shift the conductance.

4.1.2 Sigmoid activation

The second is the light-driven sigmoid activation of the NW device. There were two ways to measure the sigmoid activation: placing the beam in the centre on the NW, on-centre, and increasing the optical power in increments of a few pW or placing it off-centre and increasing the optical power quicker. The rate of increase in the second case then has to be determined for each time depending on how off-centre the beam is. The second method was used for device 4, but the problem was that it was impossible to determine at what optical power the device reacted. For this reason, the first method was used for device 5.

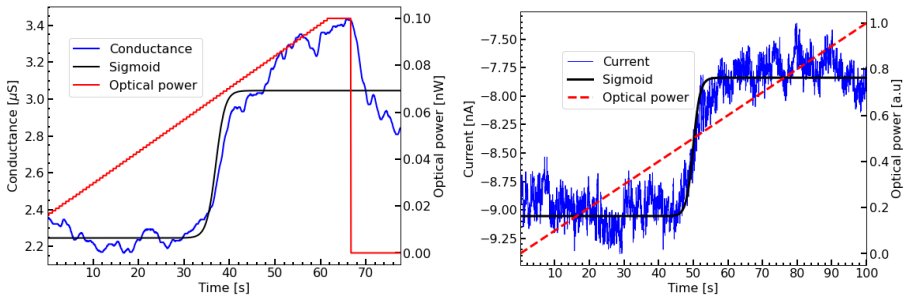

(a) (b)

Figure 17: **(a)**, the measurement for device 5 is shown with a sigmoid fit and optical power added. The blue curve shows the conductance change over time with increasing optical power where the beam is focused on the p-gate InP NW. It was measured at $V_{InP} = -1$V. **(b)**, the measurement on device 4 is shown with sigmoid fit and optical power added. However, it is impossible to determine what optical power reaches the NW at each point, thus the a.u units (arbitrary units), since the beam was focused off-centre from the NW. Furthermore, the measured unit was current, which includes a lot more noise than in (a). It was measured at $V_{InP} = -2$V

Figure 17 shows the two methods of measuring the light-driven sigmoid activation. There are many differences between these two figures. Firstly, Figure 17a was measured in conductance with the lock-in amplifier, while Figure 17b was measured in current with the Unisuko setup. Secondly, Figure 17a was measured on device 5 and Figure 17b on device 4. Finally, Figure 17a was measured with on-centre beam placement, while Figure 17b had off-centre beam placement. In the end, it was concluded that on-centre with conductance was better due to the lower noise and more precise relation between optical power and sigmoid activation. In both cases, however, the sigmoid behaviour should be observed.

A difference between these figures is that the conductance increases after the sigmoid reaches its maximum in Figure 17a. Similar results have previously been recorded on these NWs, with a linear increase instead of saturation. It is uncertain if this is a basic device issue where the conductance would continue to increase if swept to a higher maximum optical power. In simulations, a weak linear increase after sigmoid is found [9]. Another possibility would be that something in the NW shifts the conductance, such as trap states being populated/depopulated.

4.1.3 OBIC scan

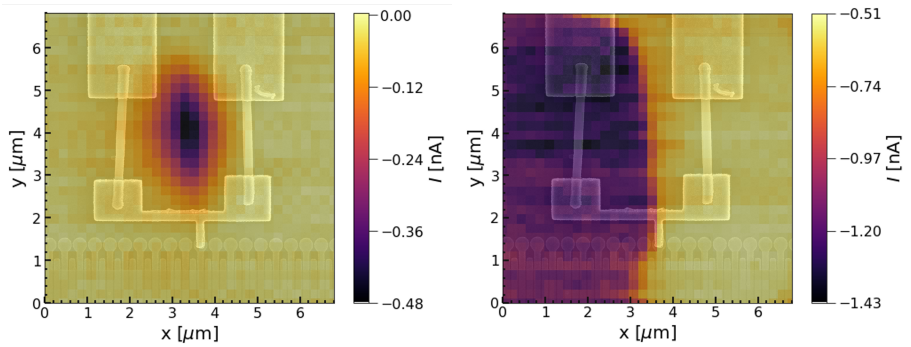

(a) I_{InP} (b) I_{InAs}

Figure 18: The OBIC scan on device 5 on sample PT9 where **(a)** shows the I_{InP} response and **(b)** shows the I_{InAs} response. The scan was measured for $V_{InP} = 0$ V and $V_{InAs} = 0$ V and an optical power of roughly 457 nW. The OBIC scan over the dark blue dotted region, see Figure 15.

The electrical response is elliptical in Figure 18a. The reason is that the optical response registered is when the two InPs conduct current as an effect of the beam. This only occurs when the optical power is strong enough, and the beam can reach both InPs simultaneously, meaning somewhere in between both of them. The exact beam power needed to achieve this response varies a bit between different setups and depends on the photo-response and capacitance of the two InP's.

Figure 18b shows the I_{InAs} response. This figure illustrates how the n and p-gates can act as inhibitory and excitatory receivers for the NW neuron. The clear line in between the InP's is indicative of the strong response from each of the InP's to the beam. The curved parts of the dividing line most likely come from the device's geometry, such as reflecting light from the contacts, etc. The far greater response in Figure 16b comes from the bias V_{InAs} applied in the measurement for Figure 16 since the I_{InAs} scales linearly at a small bias.

In Figure 16, the optical power used was 3.76 μW; in Figure 18, it was 457 nW. This was necessary to get the same optical response in I_{InP}, which can, at least partly, be attributed to the spacing between the InP NWs as illustrated in Figure 5. The conductance over the InPs in device 4 may also play a significant role. However, without this measurement for comparison, it is hard to determine the extent to which the spacing between the InPs is a contributing factor.

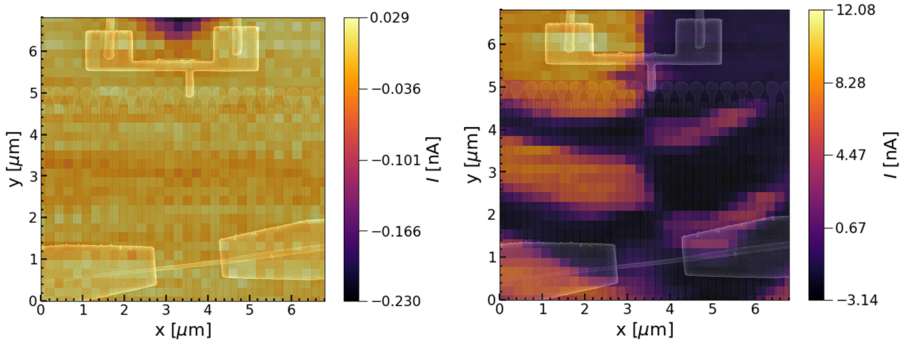

(a) I_{InP} (b) I_{InAs}

Figure 19: The OBIC scan over the InAs region for device 5 on sample PT9 where **(a)** shows the I_{InP} response and **(b)** shows the I_{InAs} response. The scan was measured for $V_{InP} = -1$V and $V_{InAs} = 5$ mV and an optical power of roughly 457 nW. The OBIC scan over the light blue region, see Figure 15

It is not that pronounced in Figure 19a, but the same elliptical pattern is visible as in Figure 18a. As expected, there is only a response when the beam sweeps between the two InP's.

It is more difficult to explain the optical response in Figure 19b. There seems to be a pronounced optical response from the InAs on I_{InAs}. The zig-zag pattern is possibly a memory effect mixed in with the optical response from the two InP's and the InAs. In this figure, we can still see the dividing line between the InP's as noted in Figure 18b, indicating that the InAs are still working as intended. The magnitude and polarity of the InP's optical response as compared to 18b comes from the difference in Gate bias between the measurements, $V_{InP} = 0$ V and $V_{InP} = -1$ V.

Another possibility is that something is happening with the beam profile. The exact beam profile is unknown, but previous measurements suggest it has some Gaussian profile. A strangely shaped beam profile would interact with the InP and the InAs unexpectedly and could cause light absorption when the beam should be in another spot. Important to notice here is that nothing of this effect is visible in Figure 18a, which indicates that it has to do with the InAS only. However, more experiments would need to be done to say anything more conclusive.

4.2 General characteristics

What follows are data measured on the two devices, 5 and 4, which tried to understand the NW neuron's general behaviour better.

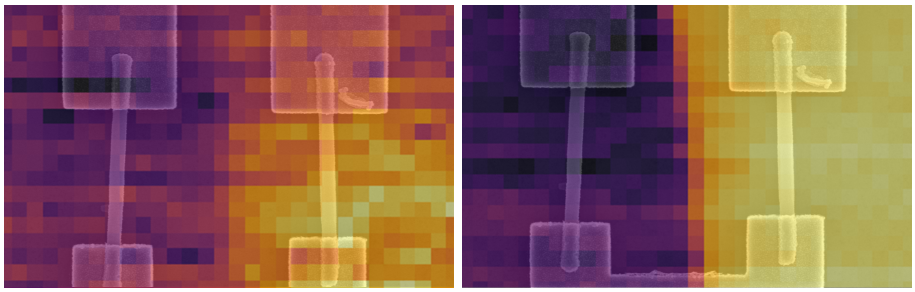

(a) I_{InAs} (b) I_{InAs}

Figure 20: The difference between the effects of $V_{InP} = 1$ V, see **(a)**, and $V_{InP} = -1$ V, see **(b)**. Both were measured with an optical power of 457 nW, but the change in current in (b) is double that in (a).

Negative bias has been used as a standard in these measurements, and the reason is best illustrated in Figure 20. In this figure, the effect on I_{InP} is compared for $V_{InP} = 1$ V and $V_{InP} = -1$ V, and it is observed that the contrast is far better for $V_{InP} = -1$ V. This can be motivated by the explanation to Figure 7 where a reverse bias, as is the case for Figure 20b with $V_{InP} = -1$ V, increases the depletion width making it easier for the NW to capture the photons.

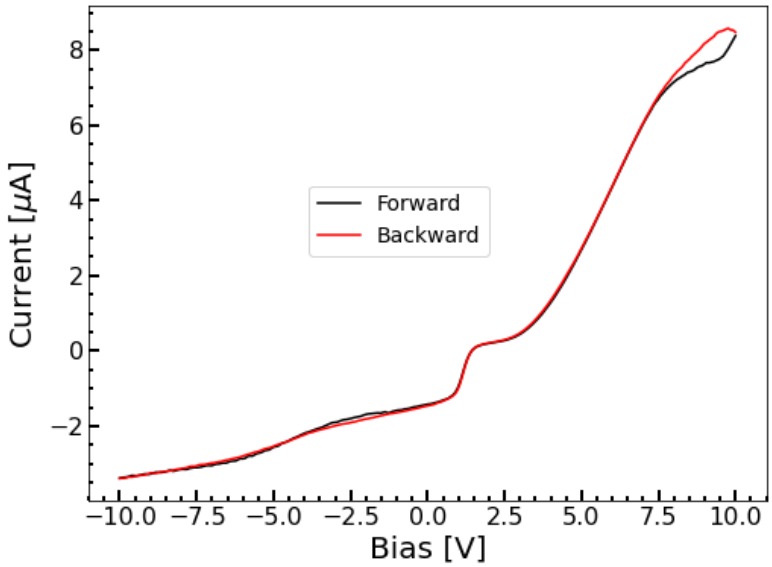

Figure 21: A IV sweep over the I_{InP} with the bias applied to the n-gate. This was done with a maximum driving current for the laser in between the NW, 170 mA

In Figure 21, the IV sweep of the InP was measured. This is not an easy

figure to interpret due to the many effects present in this circuit. It is known that in an ideal situation, Equation 2 describes an exponential increase in current with bias. There is this change present in the figure, but as illustrated in Figure 3, this is a very complex circuit and needs to be modelled to determine where the effects, such as the plateau in Figure 21, come from. This could also come from surface charges and barriers which go beyond the circuit model in Figure 3.

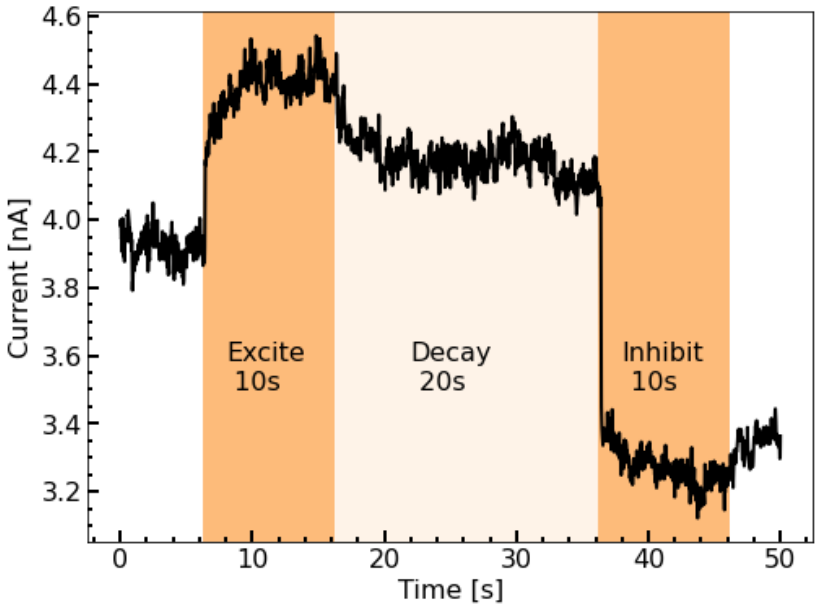

Figure 22: Current is I_{InAs}. An experiment where the activation, decay and inhibition of the NW neuron were tested for device 4 on PT9. The optical power was 10 nW and $V_{InP} = -1$ V and $V_{InAs} = 0$ V. The beam started by illuminating the p-gate and, after a rest, moved to the n-gate to inhibit the signal. All currents have switched their signs to ease the figure's interpretation.

Figure 22 tested an important aspect of the NW neurons. First is the response when the neuron is excited, then it is left so that the excited state can decay and finally, by exciting the opposite InP, the neuron is inhibited. As stated in the figure, the timescales for these operations were 10 seconds for the excitation on the p-gate, 20 seconds of darkness for the decay and 10 seconds for the inhibitions by illumination of the n-gate.

The device's general response was good, but the current level did not return to its previous level after the inhibition. This, as well as the long decay time observed in Figure 23, was probably an effect of surface and interface defects and traps. The negative bias was chosen due to its strong effect on the device's response to the illumination, as illustrated in Figure 20.

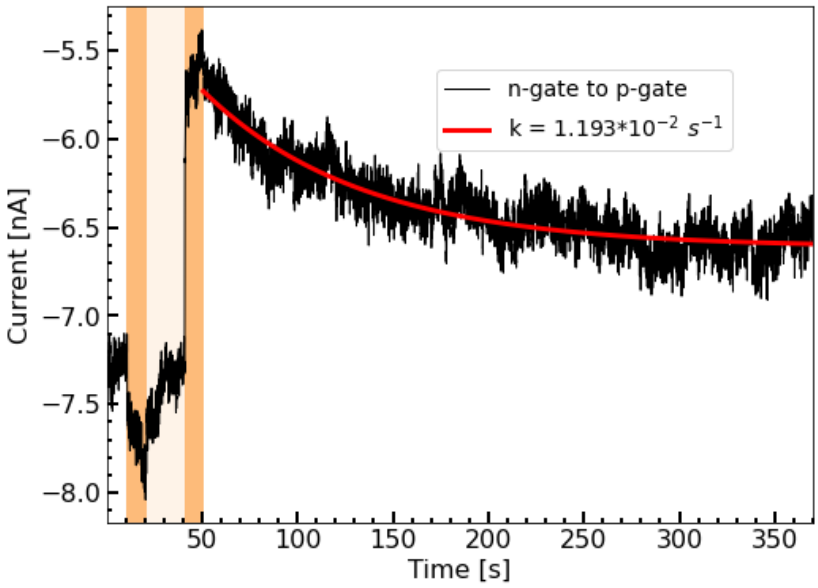

Figure 23: Current is I_{InAs}. The time of the coloured regions is the same as in Figure 22, with a long rest afterwards to capture the decay back to its original level. The n-gate to p-gate refers to how the beam was moved; it started by illuminating the n-gate and then moved to illuminating the p-gate. In this figure, the currents have not switched their signs. $V_{InP} = -2$ V and $V_{InAs} = 0$ V

Figure 23 demonstrates a significant decay time in the NW neuron. A half-life was obtained by fitting an exponential decay to the "rest" period. An exponential decay can be motivated by the argument for the DASA dye, which is that there is a thermal backreaction or decay of a charged capacitor effect in the NW.

$$t_{1/2} = \frac{log_{10}(2)}{1.193 * 10^{-2}} = 25s \tag{17}$$

The time scale of the half-life is problematic for quick measurements, but to note here is the high bias applied, $V_{InP} = -2$ V. The half-life may depend on the bias and could just as the contrast does, see Figure 20. However, it is hard to say if this is the case since insufficient data exists. It has previously been observed that trap states lead to NW hysteresis and that there is some effect on these timescales from the biasing, though how this affects the NW devices, in this case, is unclear without more experiments [24].

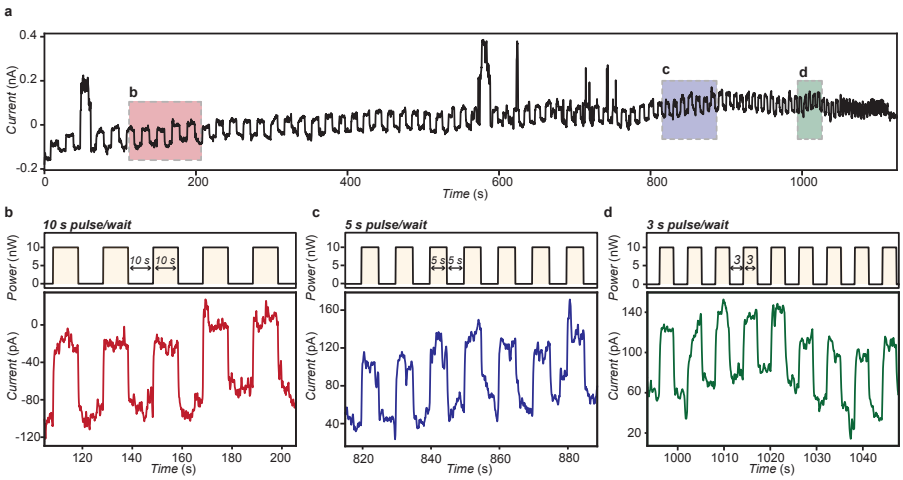

Figure 24: **(a)**, the device response to a pulse train with 10 nW peaks where the pulse duration and time between each pulse vary as a series of 10s, 9s,... 1s and finishing with 0.1s. **(b)**, a part of the 10s pulse train while **(c)** is part of the 5s pulse train and **(d)**, is part of the 3s pulse train. $V_{InP} = 0$ V and $V_{InAs} = 0$ V

There was a type of experiment that was tested and had a lot of potential, but the time needed was insufficient. This was to test pulsing behaviour on the NW neuron as seen in Figure 24. The experiment was built such that at time t_0, the laser switched on with optical power 10 nW and stayed on for t_e seconds. At $t_0 + t_e$, the laser again switched off, waited for t_w seconds, and then repeated the process to create a pulse train. Every 10 pulses, both t_e and t_w decreased with 1 second. It was then possible to compare the individual pulses for different values of $t_{e,w}$. In Figure 24 three values was looked at more closely, $t_{e,w} = 10, 5, 3$ seconds.

In Figure 24.a, there are some points at which the current reaches a much higher current level than the rest of the measurement. This can be seen at the beginning, just before 800 seconds and at some other places very shortly.

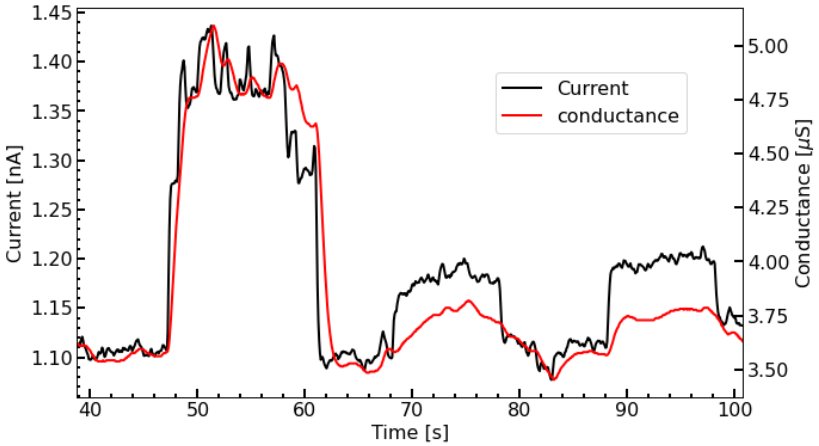

Figure 25: A zoomed-in area on the 10s pulses from Figure 24.a, where the current jumps to a current level higher than the surrounding peaks

In Figure 25, it is possible to see that even for these jumps in the current, the device still responds to the pulse the same way as in the surrounding area. This indicates that there is some shift in the NW device. This is reinforced by the fact that the same jump can also be observed in the conductance.

In this case, the conductance was also measured, but the slower response and smoother transition did not respond as clearly to the signals. This could be fixed with some tweaking of the sampling rate and would, in principle, be a preferred measurement unit since it is more consistent, less noisy and says more about the device.

This was repeated with sub-second pulses but was much more challenging to make out, and the signal-to-noise ratio was a far more significant problem. The instruments may limit the timescales and optimisations; tuning their settings might help for short pulses.

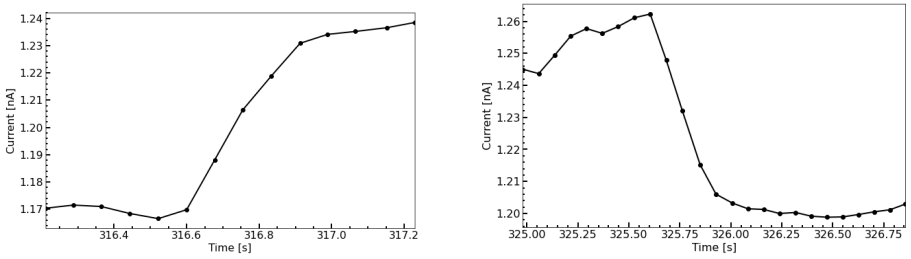

(a) (b)

Figure 26: **(a)** The excitation slope of a 9s light pulse where the black dots are the data points. **(b)** The decay slope of the same pulse

For timescales, μs or at least ms, is the goal $t_{e,w}$ to process real-world data efficiently. To reach this, more data and further analysis of the existing data are necessary to know what the optimisation needs to focus on. These optimisations could target the instruments' sampling rate and, for example, go to an all-around gate. This gate could, on the one hand, reduce surface traps, which could help the capacitance in the NW, and, on the other hand, it would give a better gate-to-InAs response.

The observed hysteresis probably results from the instruments used, such as the lock-in amplifier and the data sampling setting. It has previously been shown that the NW should have a response time of ¡1ns, see [9], which is well within the timescales needed. Even with delays in the neuron device, achieving μs response time should still be within the realm of possibility.

The mentioned hysteresis is demonstrated in Figure 26, where the response to the on/off of the light takes a few hundred ms. This can, as mentioned, probably be explained a lot by the instrument settings, but the discrepancy between this response and the one in Figure 23 is quite large. The difference could be a device variance or, as mentioned, a result of the two different V_{InP} interacting with the surface traps in the InAs. However, more measurements would be needed here to determine where this difference comes from and what contributes to the individual delays.

4.3 Molecular memory systems

In the following section, the measurements of the DASA dye are presented. First, the dye was deposited on sapphire in a polymer matrix. The measurement then consisted of illuminating under the solar simulator G2V pico and transferring it to the Bentham setup, where the transmission change could be measured over time.

4.3.1 Dye deposition parameter space

Two sets of photoswitching dye samples were prepared and measured.

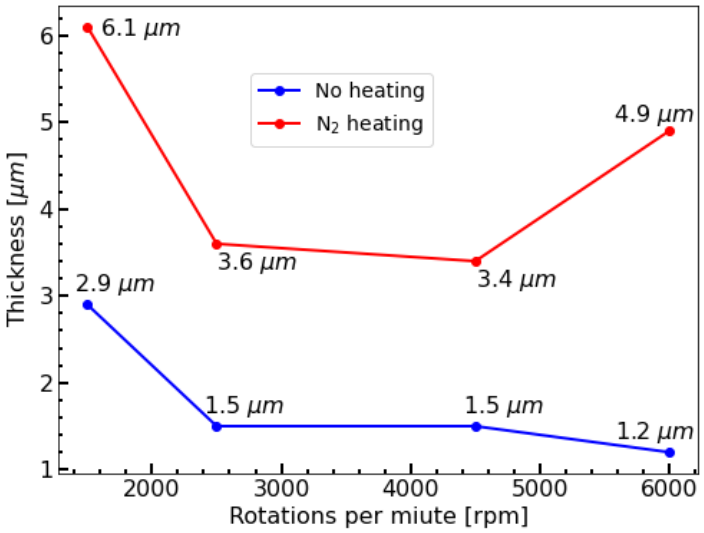

Figure 27: A plot showing how the thickness of the dye varied with spin-coating rpm between the two different batches. A Profilometer measured the thickness.

In Figure 27, the dye thickness, measured with a profilometer, as a function of rotation speed during deposition is shown. Two things stand out: there is a considerable decrease from 1500 rpm to 2500 rpm but almost no change from 2500 rpm to 4500 rpm, and for N_2 annealing, the thickness increases at 6000 rpm. For the first observation, it is unclear if this is an effect of how the samples were prepared or if this, for example, has to do with the viscosity of the dye solution. More experiments would be needed here, but since both batches have the same pattern, it could be related to the dye. Here, it is relevant to note that there is a significant difference between each batch, which shows that the thickness strongly correlates to how it is prepared. More data would be needed here to know if this is partly an effect of the annealing or if unwanted properties vary between each batch. If that is the case, then it severely affects the consistency of the dye deposition. Measuring the amount of dye to be deposited might be necessary to ensure it is always the same.

Another possibility is that the annealing has something to do with the change in thickness. This would be counter to what is expected by the annealing. The heat is expected first to expand the dye film, and when it cools down, the dye will restructure itself, limiting movement and lowering the thickness. The similar change in thickness with rpm between the batches opens the idea that the annealing could contribute to the difference in thickness between them. It is unclear why this would happen; more experiments would be needed to test if this is true.

When it comes to the increase in thickness for the 6000 N_2 sample, then it has to do with the unevenness of the surface in this case. The uneven thickness with the Bentham beam size in comparison is shown in Figure 28b. This will not be the beam's exact position but indicates how the surface is illuminated during the transmission measurement. Since the beam illuminates part of the dye, this should still be enough to measure the transmission change over time.

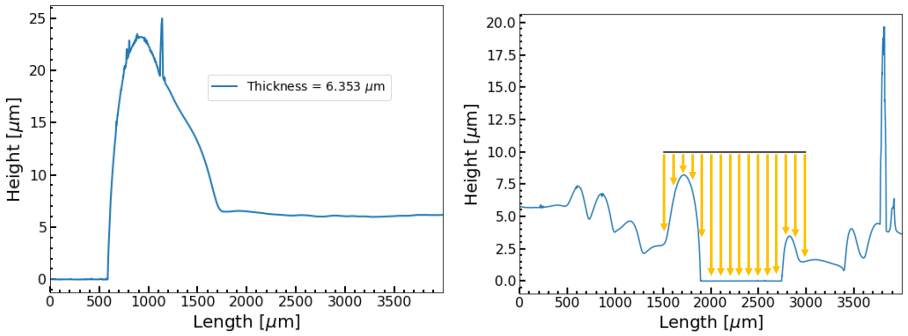

(a) (b)

Figure 28: **(a)**, the thickness of sample 1500 N_2 as measured from the edge. **(b)**, the thickness of the sample 6000 N_2. It was measured from the middle of the sample with the light beam width from the Bentham shown around the centre.

This uneven distribution is likely because the dye in this specific case was added to the sample a bit late, so the spin-coater had already reached its max velocity of 6000 rpm. In typical cases, there is a short time with low rpm when the dye can be added, after which it accelerates to its maximum value. If the dye were added too late, due to the high rpm, the dye would have difficulty sticking to the surface and thus be distributed very unevenly. Another thing that could be the reason is contamination of the sapphire, which could prevent the dye from adhering to the surface. This could be removed if the sample was first treated in a plasma etcher before placing it in the spin-coater.

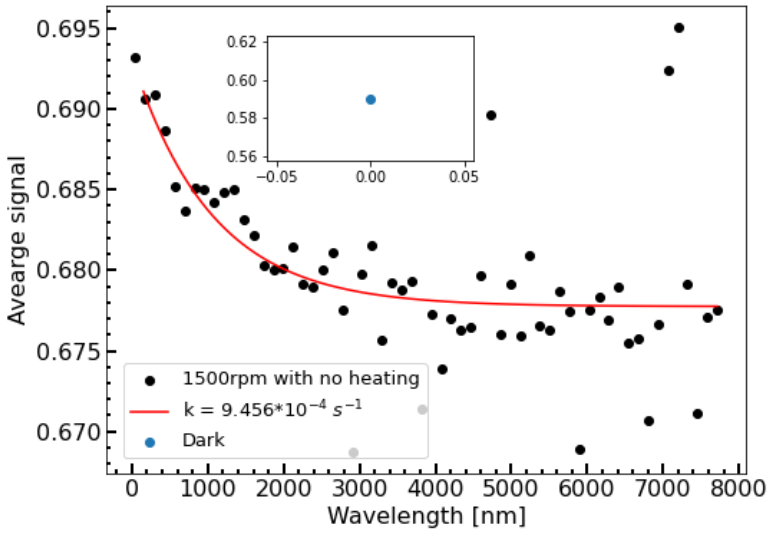

Figure 29: The fit for the data obtained from the transmission measurement 1500 with no heating. The Dark measurement was done before the illumination and can be considered a measurement of this sample's lowest possible transmission, T_0. For this measurement, 7 minutes of illumination, a total irradiance of 1.2 mW/cm^2 and a sub 0.74 mm aperture were used in the Bentham.

From this fit, the time constant is

$$k = 9.456 * 10^{-4} s^{-1} \tag{18}$$

Which gives a half-life of

$$t_{1/2} = 318s \tag{19}$$

As mentioned, AP-048 in PAMS has previously been observed to have a half-life of around 160 s, about half the value measured for sample 1500 with no heating, see Equation 19. It is hard to say if this is an effect of the noise, if it has to do with the deposition or if it is specific to this sample since only this sample in the no-heating batch could have the kinetic model fitted to its data.

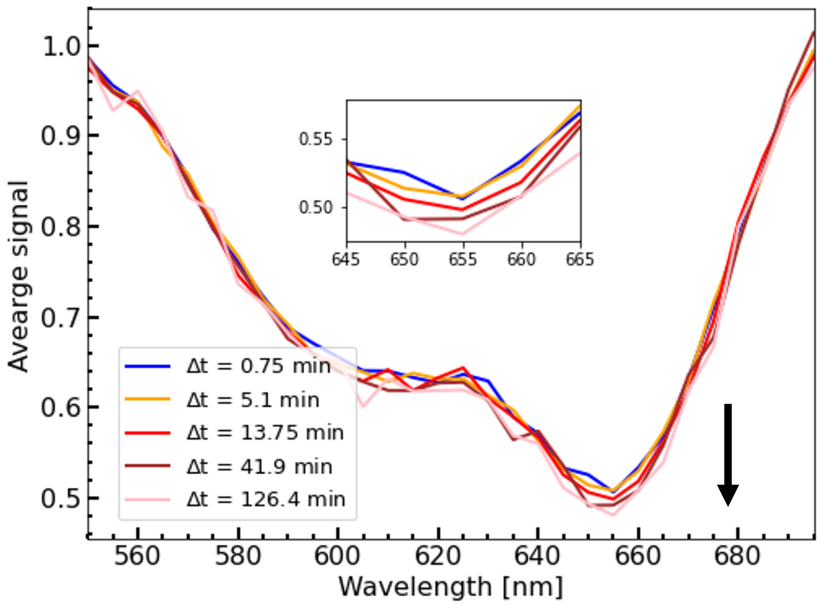

Figure 30: Some chosen transmittance lines for sample 1500 with no heating where the black arrow indicates how the transmittance changes over time. These lines were chosen to illustrate the difference between the transmittance lines for sample 1500 N_2 and 1500 with no heating.

The small, if even noticeable, change over time in Figure 30 shows the apparent weak effect of the 7-minute illumination in the solar simulator G2V pico. The overlapping and uneven lines and the slight change explain the noisy behaviour in Figure **??**.

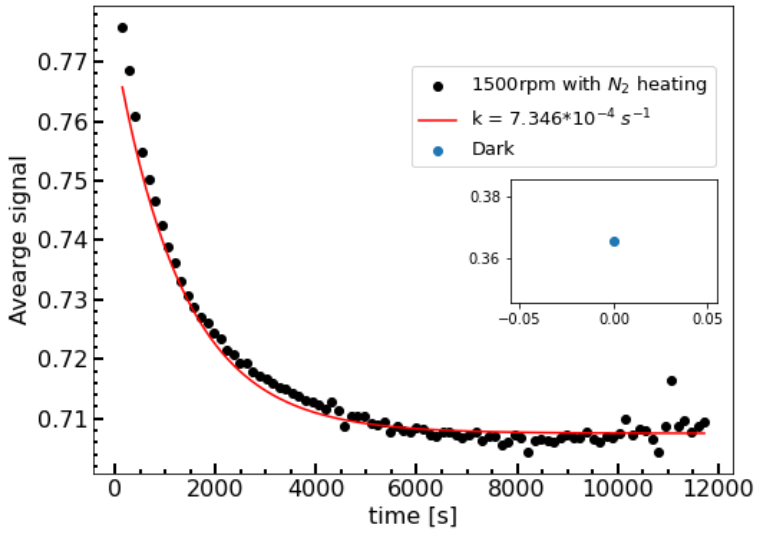

Figure 31: The fit for the data obtained from the transmission measurement for 1500 N_2. The Dark measurement was done before the illumination and can be considered a measurement of this sample's lowest possible transmission, T_0. For this measurement, 15 minutes of illumination and a 1.5 mm aperture were used.

From this fit, the time constant is

$$k = 7.346 * 10^{-4} s^{-1} \tag{20}$$

Which gives the half-life of

$$t_{1/2} = 410s \tag{21}$$

Compared to Figure **??**, this is a better fit with far less noise. This difference could be attributed to the change in aperture to 1.5 mm and the longer illumination under the solar simulator, here, 15 minutes. The longer illumination can best be seen in the difference between the dark measurement and the beginning of the decay, ≈0.36 versus ≈0.78 average signal. This can be compared to the corresponding values in Figure **??** where the dark measurement was ≈0.59 while the beginning of the decay was ≈0.69.

The half-life measured in Equation 21 is longer, which is expected, than what was obtained for 1500 with no heating. The longer half-life comes from the fact that during annealing, the dye will first expand and, when later cooling down, the molecules will rearrange in a more tightly packed structure. The structural shift for the dye going from M state to GS will thus require more energy and consequently take longer. This longer half-life is attributed to the annealing, where the atmosphere may have an additional effect, but their contributions are impossible to separate from this limited data.

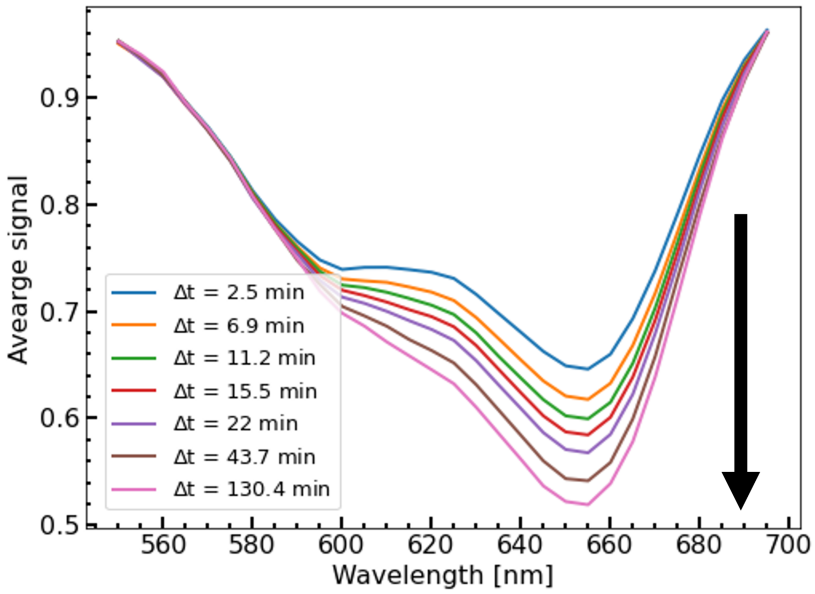

Figure 32: Some chosen transmittance lines for sample 1500 N_2 where the black arrow indicates how the transmittance changes over time.

In the case of Figure 32, there is a clear and smooth change over time in transmission. This result further motivated the change to the 1.5 mm aperture, especially compared to the previously mentioned result of Figure 30.

Much of the data obtained from the transmission measurements did not give a clear decay pattern, as seen in Figure 31, but exhibited a linear increase in average signal. A behaviour that is opposite to what is predicted by the dye kinetic model.

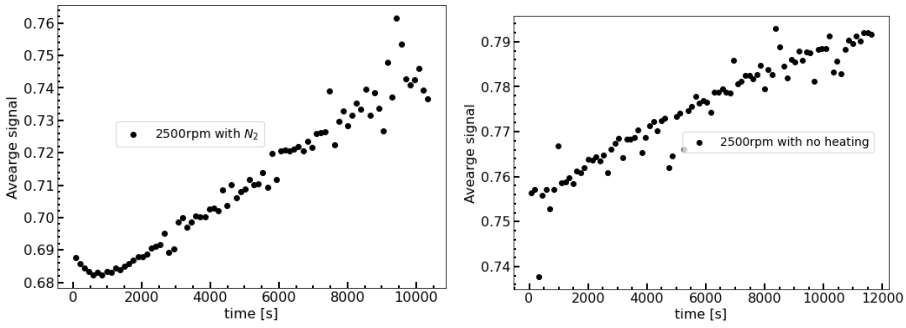

(a) (b)

Figure 33: **(a)**, the transmission measurement of 2500 N_2. **(b)**, the transmission measurement 2500 with no heating.

Figure 33 shows two transmission measurements where the transmission increases over time instead of decaying exponentially. The fact that the decay disappears after the first few points in Figure 33a and starts to grow again could indicate that the excitation is not as power-dependent as it is time-dependent. If it were strongly power-dependent, it would be expected that a more pronounced and prolonged initial decay would appear with twice the optical power in the solar simulator. This is because the c_{GS} population should be more exhausted such that fewer new molecules can be excited while there at the same time are more c_M with exponential decay. This was tested; the results are presented in Figure **??**.

What argues against this theory is that linear increase in transmission goes beyond the tail maximum. As mentioned, this means more c_M and should contribute to an increasingly dominant exponential decay.

Figure 33b shows no initial decay pattern and only a linear increase. This could mean that it depends on annealing or thickness, but it is unclear why it would be either case.

Most samples, with only exceptions 1500 N_2 and 1500 with no heating, showed this linear increase and more measurements were motivated. With the sample 2500 N_2 showing the initial decay, being the thickest after 1500 N_2 and closest to 1500 with no heating in thickness, it was decided that further measurements should be conducted on this sample.

One of these experiments was to keep the exposure time the same but increase the optical power from 500 to 1000 LED power, increasing the total irradiance from 1.2 mW/cm^2 to 2.4 mW/cm^2. Another was to illuminate at the same irradiance as before but increase the time from 15 to 30 minutes. These results provided some changes from the previous measurement but did not appear to fix the issue of the transmission increasing over time.

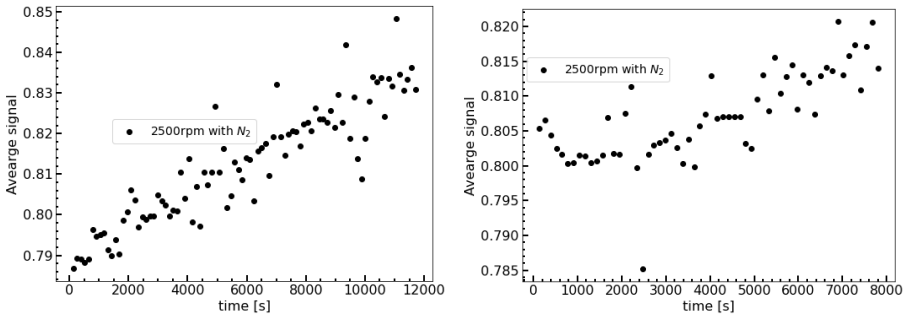

(a) (b)

Figure 34: The same device as in figure 33a, 2500 N_2 is measured but with some changes to the solar simulator illumination. **(a)**, the intensity of the solar simulator is doubled with all else as standard. **(b)**, the illumination time of the solar simulator is doubled with all else as standard.

There are some changes when comparing Figure 34a and Figure 33a. Most notably, the initial decay in Figure 33a has disappeared. This is a bit surprising since the tail should indicate that enough photoswitching dye is excited such that the decay dominates the kinetics.

Another difference between the figures is the transmission change. In Figure 34a, the transmission is roughly 0.1 average signal higher than in 33a. This significant change does not necessarily contradict the earlier assumption about weak power dependence. In the theoretical limit, the transmission should be close to 1 when all the photoswitching dye is excited since it is normalised to the sapphire substrate. The intensity change affects the transmission, but considering the doubled irradiance, this effect is not very strong.

In Figure 34b, there is still some initial decay, but otherwise, only the rate at which the transmission changes differs from Figure 34a. This indicates that the increase in transmission does not depend on the solar simulator illumination. Thus, the theory of why the transmission is linearly increasing instead of exponentially decreasing changed. It was now reasoned that this effect was the Bentham continuing bleaching of the sample over time in the transmission measurement.

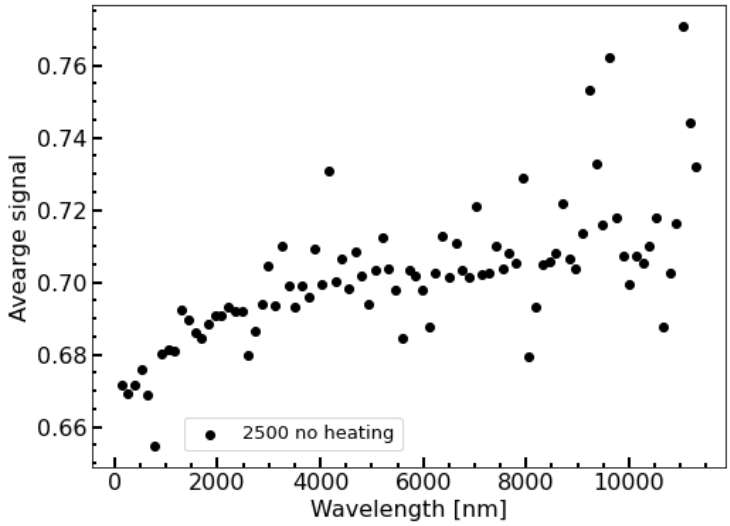

Figure 35: A measurement on sample 2500 N_2 with aperture sub 0.74 mm.

In Figure 35, the sub 0.74 mm aperture was used, and the result was similar to Figure 34b but with more noise. A saturation in transmission after around 3000 seconds strengthens the theory that the Bentham bleached the sample since a smaller aperture would let through less light. The initial increase in transmission could indicate that the sample was bleached until 3000 seconds until a stable state was reached.

A few more measurements were conducted to determine whether the Bentham or long-time scales were the problem. However, further measurements used the

1.5 mm aperture because, as previously stated, it had less noise.

Firstly, sample 2500 N_2 was illuminated with the standard measurement setup. A longer measurement, this time 5.5 hours, was done where the results are visible in Figure 36.

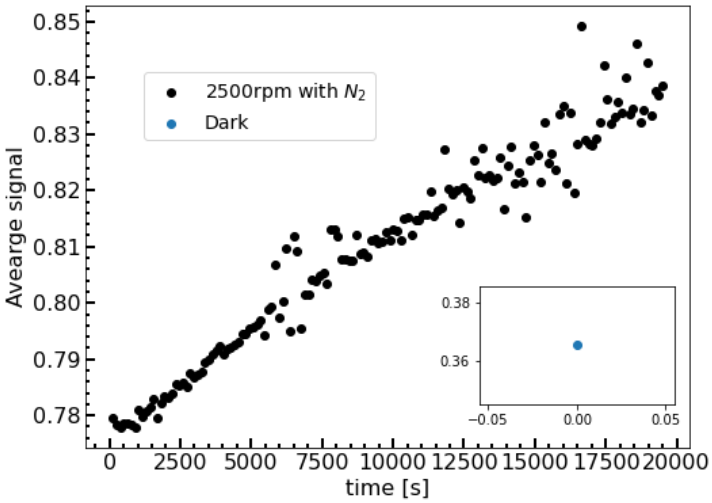

Figure 36: Sample 2500 N_2 was illuminated by the standard program and measured over a long time, 5.5 hours.

The results show that no difference from before can be noticed from Figure 34a and that there is still linearly increasing transmission with time. Thus, an hour after this measurement was finished, the sample was again bleached by the same process, and a 16-hour measurement began. The results are visible in Figure 37.

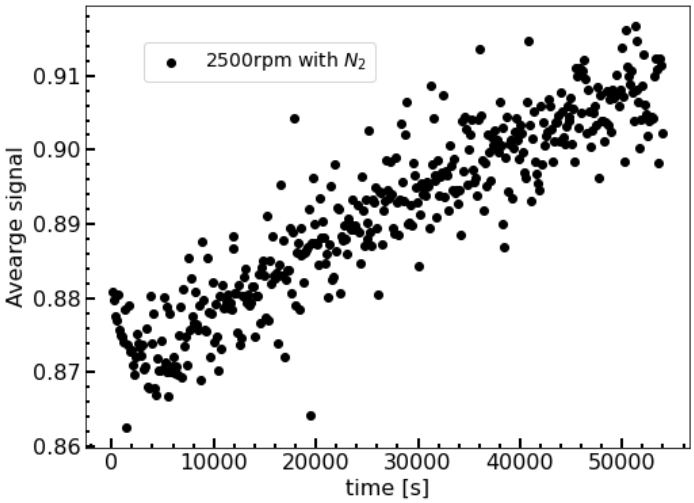

Figure 37: An hour after the measurements in Figure 36, the sample was again illuminated and measured for around 16 hours.

The pattern remained even after these 16 hours, with a linear transmission increase.

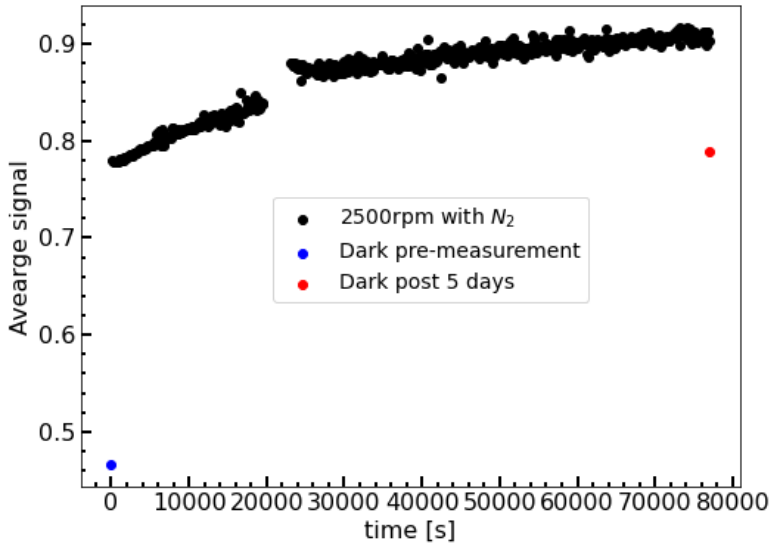

Figure 38: The combination of Figure 36 and Figure 37 with the first dark measurement included. A second dark measurement was done 5 days later and included as well.

When looking at the combination of the results in Figure 38, it is seen that the increase in transmission slows down as the c_{GS} population are exhausted. However, The decay cannot be observed, and combined with the dark measurement done 5 days later, there are two possible explanations.

One is that what is observed is a very long decay time with a half-life of days. This could be tested with several dark measurements a few hours after each other over days, but it was not done in this project. This explanation seems a bit far-fetched since the sample 1500 N_2 fitted to the kinetic model with a half-life of around 7 minutes. The drastic change in half-life between these samples when, at least in theory, only the rpm has changed from 1500 to 2500 is hard to motivate.

Another possibility is that repeated measurements and bleaching by Bentham have irreversibly bleached a significant portion of the dye. In Figure 38, the difference between "Dark pre-measurement" and "Dark post 5 days" is 0.32, which is a 70% increase from the "Dark pre-measurement", which has a value of 0.47. Note that the "Dark pre-measurement" was done before any measurements were taken on sample 2500 N_2. Adding to this is the previously mentioned fact that considering the half-life of 1500 N_2, it is expected that at the time of "Dark post 5 days", all the c_M population should be exhausted from thermal decay. The irreversibly bleached molecules can also result from the time from deposition to the last measurement, old dye or something similar. More data is needed here to know what happens. However, this result indicates that long continuous measurements irreversibly bleach a significant portion of the dye.

This irreversible bleaching can likely be mitigated if the dye isn't continuously

bleached during transmission measurement. The less the molecules are excited, the less likely they are to bleach irreversibly. This is the case when decay dominates, and a longer lifetime of the sample and dye would be expected than observed in this project.

If it is assumed that the c_M population is entirely exhausted from thermal decay at "Dark post 5 days", then it gives some limitations to the half-life but does not say much about what to expect it to be.

After finishing the measurement in Figure 37, a picture was taken of the sample and, as can be seen in Figure 39, an area in the middle of the sample can be observed where it has been more bleached than in the surroundings.

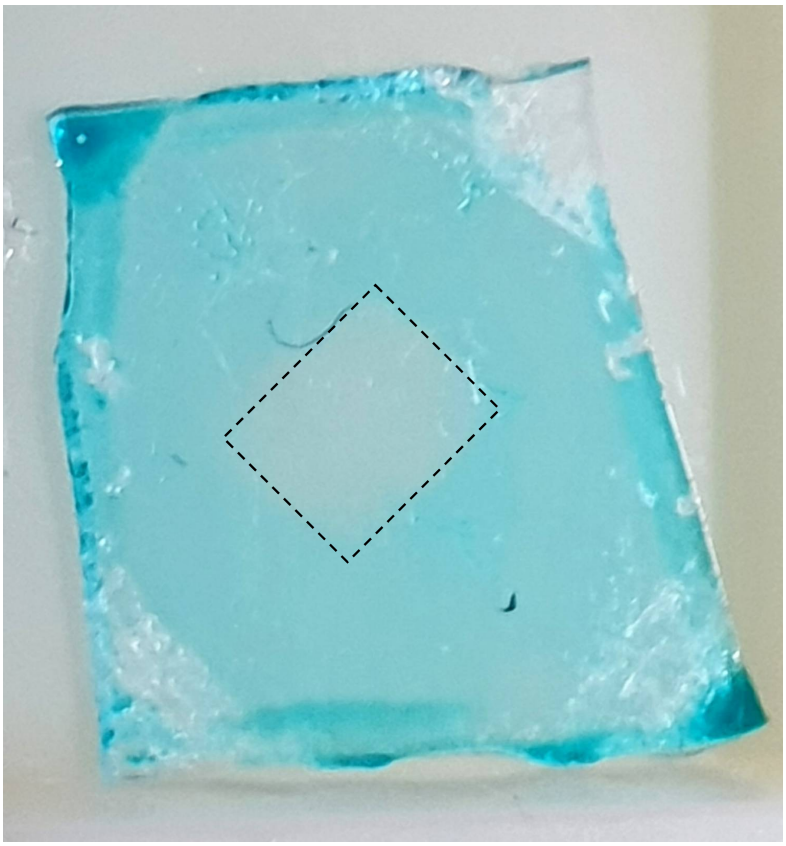

Figure 39: A photo of the dye on sapphire sample 2500 N_2 after measuring for 16 hours. The dotted rectangle marks the visibly bleached area in the middle.

This strongly reinforces the theory that the linear increase in transmission comes from the Bentham. The square shape also coincides with how the beam spot is shaped.

5 Conclusion

5.1 First research question

Let's first refresh the memory of the first research question.
How does illumination and gate bias influence the nanowire-based artificial neuron?

- Using a linearly increasing optical power focused on one InP gave a sigmoid activation in the I_{InAs}. This shows that the NW neuron can implement this necessary effect from the biological neuron without optimisations. A larger response when gating using the InPs is desired since that makes the output signal more robust. However, many optimisations remain, such as the passivisation of surface traps.

- Through an OBIC scan and an excite-decay-inhibit type measurement, it was possible to simulate the excitation and inhibition of the NW neuron. This shows that the NW neuron can implement another necessary component of the biological neuron even as the inhibition and excitation occur at the same wavelengths.

- The electrical performance was determined through a conductance measurement on the InAs. The conductance varies a bit depending on when the measurement is done. This variance is not problematic since the change in conductance is interesting for measurements but could be explored further. It probably depends on exposure to the atmosphere, surface traps and effects in the contacts.

- The OBIC scan on the InAs indicated an unwanted photoelectric effect from the InAs on I_{InAs}. This will be fixed in the final version with an all-around gate. Before this gate is used, something else might be needed to limit the InAs's photoelectric effect.

- Focusing the beam on an InP and pulsing the light with fixed pulse and rest times showed good response for down to single-second time-scales.

- Looking at the NW's excitation and decay response time indicates a limit to the pulse time scales at a few hundred milliseconds. More work must be done here to bring it down to the desired ms/μs. One thing contributing to the slow response could be the hysteresis effect of surface traps or the inbuilt memory in the gate. It could also be an effect of the time constant chosen for the sampling rate in the measurement setup.

5.2 Second research question

The second research question is as follows.
How does the depositing of the photoswitching dye influence its properties?

- As expected, a higher spin-coating rpm leads to a thinner dye film, but it does not seem linear with rpm. There is a sharp drop in thickness from 1500 to 2500 rpm, followed by almost no change from 2500 up to 6000 rpm. More tests would be needed here to understand this trend in more detail.

- For the annealed batch, there was an outlier in the 6000 N_2 sample where the thickness increased again. This could, however, be explained by a very uneven surface thickness, possibly originating from organic residue or other particle contamination on the surface. This could be avoided in future experiments by treating the sapphire in a plasma etcher for sub-15 seconds.

- A significant thickness difference but similar rpm dependence between the thin film batches suggests an unexpected increase in thickness from annealing. No conclusion can, however, be drawn regarding this since only two batches of dye were compared.

- Since the annealing also included N_2 atmosphere, it is impossible to determine if the increased thickness is a fluke from deposition, an effect of annealing, or influenced by N_2 atmosphere. Possibly a combination of all three.

- Two out of eight samples conformed to the kinetic model, 1500 with no heating and 1500 N_2, with the annealing sample exhibiting slower kinetics. 1500 with no heating was measured to have a half-life of 318 seconds, while 1500 N_2 had a half-life of 410 seconds. Previously measured data by Abbey M. Philip was 160 s. The difference between the samples was expected due to the presence or absence of annealing, but the significant difference compared to Abbey M. Philip's data was unexpected. Ultimately, the data was insufficient to arrive at any definitive conclusions.

- For sample 2500 N_2, there was an apparent increase in permanently bleached dye molecules with subsequent measurements. This expected result reveals that much of the dye permanently bleach over time. However, whether this is primarily due to the continuous bleaching during measurements or an unavoidable effect over time is uncertain.

- For the same sample, 2500 N_2, it is impossible to know the half-life with any accuracy, but assuming that all of the c_M is exhausted at "Dark post 5 days", then it puts some limitations to it. However, this is the only clue to the half-life of any sample other than 1500 with no heating and 1500 N_2.

- A linear increase in transmission during the measurements for most samples and a visibly bleached spot on sample 2500 N_2 comparable to Bentham's beam spot size strongly suggests that the samples are bleached during transmission measurement.

- When comparing the thickness of the samples with the aperture size, a pattern became apparent. Thinner samples required a smaller aperture, but using a small aperture led to a poor signal-to-noise ratio. The aperture size,

which correlates with incident intensity, must be adjusted for the sample's thickness to prevent bleaching during measurement.

5.3 Outlook

Continuing this research will lead to moving into mixing dyes. There are options for mixing dyes of the same absorption peak wavelength but with different kinetics to achieve different time scales for the memory of the weights. Another thing that will be important to move into and research is mixing dyes of different wavelengths. The main thing to try out for these measurements is how the different dye concentrations affect the kinetics. Something else would be to see how many different dyes could be mixed with noticeable results. The motivation for this would be memory with different timescales. An example could be implementing an internal clock with days, weeks or even a year.

When further exploring the parameter space of depositing the dyes, heating will be interesting. This is also important when evaluating how much the heating or N_2 affects the thickness. Trying different atmospheres and using plasma etching before depositing the dye would also be interesting. Etching could significantly improve dye adhesion to the sapphire. All of these do, however, depend on getting a result from the transmittance measurements. For this, it will be essential to understand how the aperture size, or the incident intensity, is related to the bleaching of the sample at different thicknesses.

Given some samples' potentially long half-life, elevating the temperature of the sample during measurement could be helpful. With a higher temperature, the temperature-dependent decay would speed up, and even long half-lives could be observed quickly.

As we advance, several exciting things regarding nanowires and artificial neurons are to be considered. The first one might be to get a good understanding of the beam profile for the laser diode so that intensity can be calculated and used in the measurements. This will make it easier to replicate and test the previous measurements.

A few things need to be improved in the excite-decay-inhibit test. One of these would be to try to send excitatory and inhibitory signals overlapping in time. Another would be how long the decay can last, where there is still an inhibiting effect. Understanding how the hysteresis depends on the V_{InP} bias would also be interesting.

For sigmoid activation, it will be necessary to push the boundaries of how long it can retain the signal, how slow the sigmoid can be activated, and if it can be activated by accumulating signals. The purpose of these slow sigmoids is to see how long in between the signals it is possible to have and still get a sigmoid activation. Another thing to try for sigmoid activation is to activate it by short trains of pulses instead of continuous illumination. By this, it would be possible to see if the signals between two communicating NW neurons can be used or if something needs to be fixed.

In the case of the OBIC scan, it could be interesting to have the heatmap measure the conductance response instead of the current. Before the all-around gate is implemented, some light blockers may be needed for the InAs. This could also alleviate surface traps, possibly improving the overall performance.

The pulse train has great potential since it can extract the kinetics of the nanowire neurons' response to excitatory signals and their decay. Exploring how these change with different parameters, such as bias, optical power, pulse/rest time, etc., could help understand the limitations in the neuron's time domain and how to optimise them.

To understand the nanowire neuron, it will be necessary to model the InP and gate circuit. This would allow an explanation of the IV measurement and knowledge of how the individual components work. Together with this, it would be interesting to probe the individual InPs. Testing different ways to pacify the surface traps in the future will also be essential. Some plans have already been lifted in the InsectNeuroNano project, such as covering the entire sample in an oxide or dye. Eventually, a combination of NW neurons, dye and waveguides will have to coexist on the same plane and beginning to test how these components work together will be necessary.

A subject not touched on in this project is exploring the effects heating or cooling would have on the nanowire neuron. This could be significant in detecting and emitting photons, noise levels, and optical power dependence.

A Appendix

A list of relevant measurements during the project that were not included in the results is presented below.

Transmission in samples prior to bleaching

The normalised transmission for all the samples

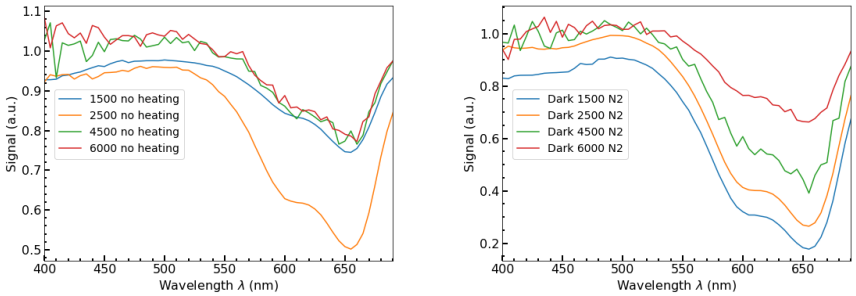

(a) (b)

Figure 40: The transmission, normalised against the blank sapphire sample, for the dark measurement of the thin film batch which wasn't annealed and the one that was annealed in N_2

The fact that 1500 with no heating has the same transmission as 4500 and 6000 with no heating despite being much thicker is probably because this measurement was done much later. This sample worked with the initial measurement at a sub 0.74 mm aperture, which meant that a dark measurement with a 1.5 aperture was needed only at the end.

Transmission measurements

Here are the transmission measurements not presented in the result, 4500 and 6000 for N_2 and no heating.

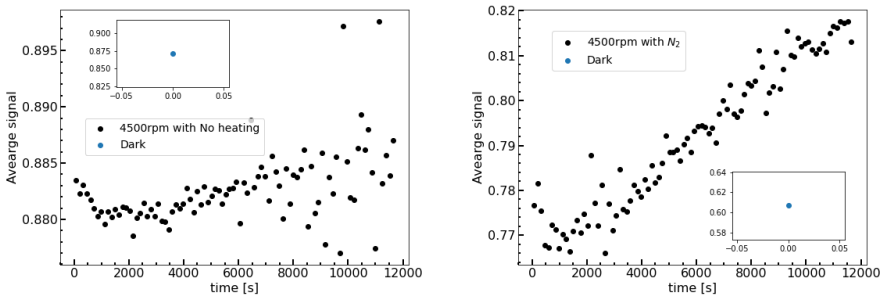

(a) (b)

Figure 41: The transmission change over time for sample 4500 with no heating for **(a)** and N_2 for **(b)**

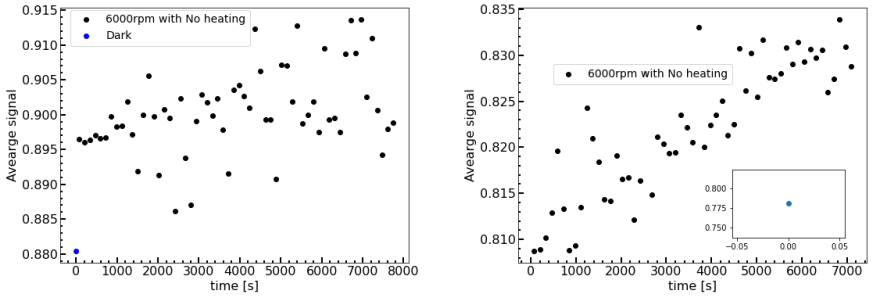

(a) (b)

Figure 42: The transmission change over time for sample 6000 with no heating for **(a)** and N_2 for **(b)**

Optical power measurements

The measured Optical power per driving current that was used to make the linear increase in optical power for the sigmoid measurements.

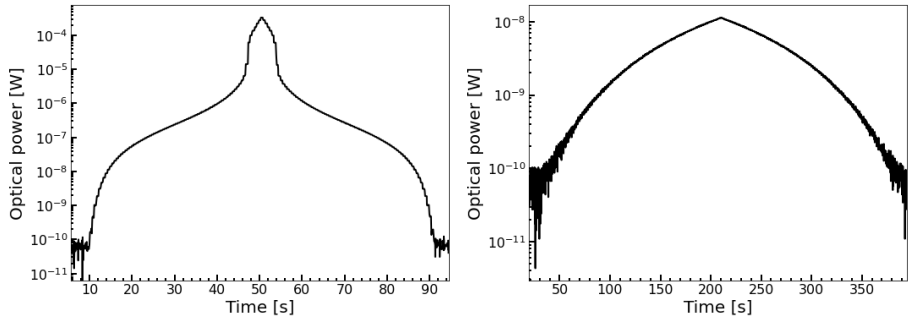

(a) (b)

Figure 43: Two figures showing a linear increase in driving current while measuring the total optical power of the laser. A relation was extracted between driving current and optical power so that the optical power could be swept linearly for later experiments. **(a)**, optical power measurement where the driving current on the laser diode was swept from 0 to 80 mA. Each step in the graph represents a step of 1 mA, whereas the first step, from 0 to 1 mA, can not be seen due to insufficient power. **(b)**, optical power measurement where the driving current on the laser diode was swept from 0 to 10 mA. The step size here was much smaller and slower than in Figure 43a

Other Sigmoid curves

Further sigmoid curves measured with different time scales

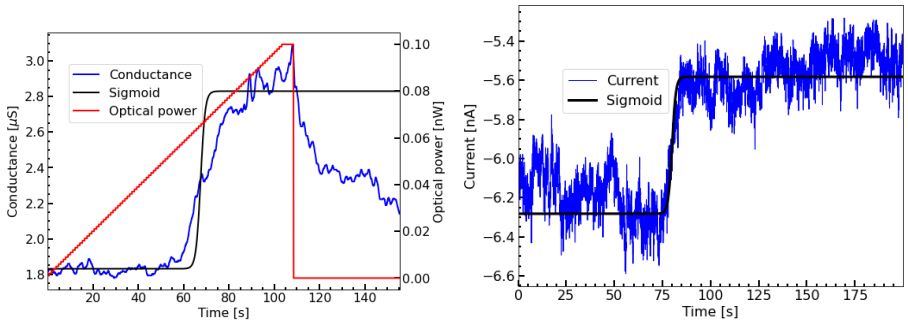

(a) (b)

Figure 44: **(a)**, a sigmoid curve on device 5 with 140 s instead of 70 s as in Figure 17a. In this case, there is also this continuous increase as in Figure 17a. **(b)**, a sigmoid curve on device 4 where the optical power isn't marked due to it not being known if the saturation is from rest at max optical power or if there was a constant increase but no more response.

Sub-second pulse train

A measurement of the pulse train for 1, 0.9, 0.8, ... 0.1-second pulses

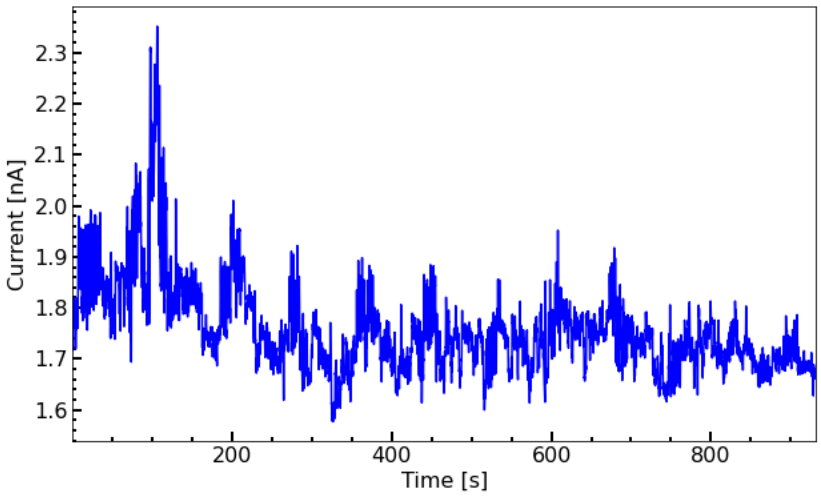

Figure 45: The sub-second pulse train was measured but not used since the noise was far too prevalent in this measurement. The measurement was done with $t_w = t_e + 1$s and a 60s wait between each 10 set of pulses.

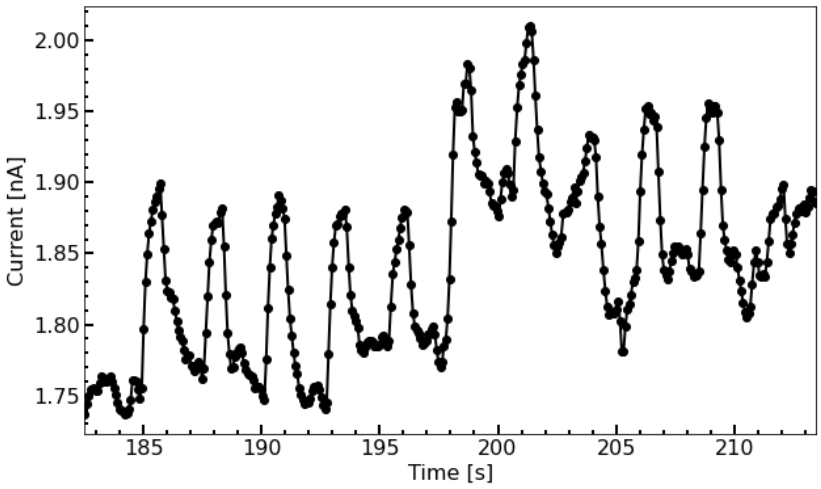

Figure 46: The 0.8 s pulse train from Figure 45.

IV curves

Additional IV measurements were done on device 5

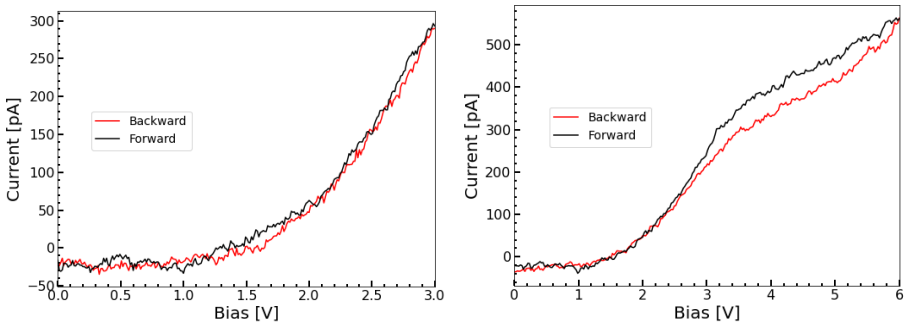

(a) (b)

Figure 47: The IV curve of device 5 with no light incident on the sample. **(a)** goes from 0 to 3V while **(b)** goes from 0 to 6V. (a) illustrates the expected exponential behaviour from Equation 2. Both of these are measured on I_{InP}.

References

1. Patel, R. N., Kempenaers, J. & Heinze, S. Vector navigation in walking bumblebees. *Current Biology* **32,** 2871–2883.e4. ISSN: 0960-9822. https://www.sciencedirect.com/science/article/pii/S0960982222007692 (2022).
2. de Vries, A. The growing energy footprint of artificial intelligence. *Joule* **7,** 2191–2194. ISSN: 2542-4351. https://www.sciencedirect.com/science/article/pii/S2542435123003653 (2023).
3. Trihinas, D., Thamsen, L., Beilharz, J. & Symeonides, M. *Towards energy consumption and carbon footprint testing for ai-driven iot services* in *2022 IEEE International Conference on Cloud Engineering (IC2E)* (2022), 29–35.
4. Marković, D., Mizrahi, A., Querlioz, D. & Grollier, J. Physics for neuromorphic computing. *Nature Reviews Physics* **2,** 499–510 (2020).
5. Arikpo, I., Ogban, F. & Eteng, I. Von neumann architecture and modern computers. *Global Journal of Mathematical Sciences* **6,** 97–103 (2007).
6. *Insect-Brain inspired Neuromorphic Nanophotonics — InsectNeuroNano Project — Fact Sheet — HORIZON — CORDIS — European Commission — cordis.europa.eu* https://cordis.europa.eu/project/id/101046790. [Accessed 02-06-2024].
7. Basheer, I. & Hajmeer, M. Artificial neural networks: fundamentals, computing, design, and application. *Journal of Microbiological Methods* **43.** Neural Computting in Micrbiology, 3–31. ISSN: 0167-7012. https://www.sciencedirect.com/science/article/pii/S0167701200002013 (2000).
8. Winge, D. O. *et al.* Implementing an Insect Brain Computational Circuit Using III–V Nanowire Components in a Single Shared Waveguide Optical Network. *ACS Photonics* **7.** PMID: 33123615, 2787–2798. eprint: https://doi.org/10.1021/acsphotonics.0c01003. https://doi.org/10.1021/acsphotonics.0c01003 (2020).
9. Winge, D., Borgström, M., Lind, E. & Mikkelsen, A. Artificial nanophotonic neuron with internal memory for biologically inspired and reservoir network computing. *Neuromorphic Computing and Engineering* **3,** 034011 (2023).
10. Kjellberg Jensen, Thomas. *Optical Communication using Nanowires and Molecular Memory Systems* eng. Master's thesis (Lund University, 2024).
11. Simon M. Sze, K. K. N. *Semiconductor Devices Physics and Technology* 3rd ed. Chap. 1 (Wiley, 2010).
12. Zelenina, A. *Silicon nanocrystals in various dielectric matrices: Structural and optical properties* PhD thesis (Albert-Ludwigs-Universität Freiburg, Jan. 2015).
13. Balakrishnan, N. *Novel approaches to the fabrication of nanoscale devices* PhD thesis (The University of Nottingham, July 2015).

14. Simon M. Sze, K. K. N. *Semiconductor Devices Physics and Technology* 3rd ed. Chap. 3 (Wiley, 2010).

15. Otnes, G. *et al.* Understanding InP Nanowire Array Solar Cell Performance by Nanoprobe-Enabled Single Nanowire Measurements. *Nano Letters* **18** (Apr. 2018).

16. Dayeh, S. A. *et al.* High electron mobility InAs nanowire field-effect transistors. *small* **3,** 326–332 (2007).

17. Hsu, C.-Y. *et al.* Nanowires Properties and Applications: A Review Study. *South African Journal of Chemical Engineering* **46,** 286–311. ISSN: 1026-9185. https://www.sciencedirect.com/science/article/pii/S102691852300077X (2023).

18. Alexander-Webber, J. A. *et al.* Engineering the Photoresponse of InAs Nanowires. *ACS Applied Materials & Interfaces* **9.** PMID: 29171260, 43993–44000. eprint: https://doi.org/10.1021/acsami.7b14415. https://doi.org/10.1021/acsami.7b14415 (2017).

19. Wernersson, L.-E., Thelander, C., Lind, E. & Samuelson, L. III-V Nanowires—Extending a Narrowing Road. *Proceedings of the IEEE* **98,** 2047–2060 (2010).

20. in. *Molecular Fluorescence* 20–33 (John Wiley Sons, Ltd, 2001). ISBN: 9783527600243. eprint: https://onlinelibrary.wiley.com/doi/pdf/10.1002/3527600248.ch2. https://onlinelibrary.wiley.com/doi/abs/10.1002/3527600248.ch2.

21. Helmy, S., Oh, S., Leibfarth, F. A., Hawker, C. J. & Read de Alaniz, J. Design and Synthesis of Donor–Acceptor Stenhouse Adducts: A Visible Light Photoswitch Derived from Furfural. *The Journal of Organic Chemistry* **79.** PMID: 25390619, 11316–11329. eprint: https://doi.org/10.1021/jo502206g. https://doi.org/10.1021/jo502206g (2014).

22. Ceberg, Nils and Säll Nilsson, Jacob. *Modelling photoswitching dye memory for path integration* eng. Master's thesis. 2022.

23. *Home &x2014; QCoDeS 0.46.0.dev337 documentation — microsoft.github.io* https://microsoft.github.io/Qcodes/. [Accessed 01-06-2024].

24. Hanrath, T. & Korgel, B. A. Influence of surface states on electron transport through intrinsic Ge nanowires. *The Journal of Physical Chemistry B* **109,** 5518–5524 (2005).